micro

MDPI

Article

Nanotech Trojan Horse: Chitosan–ZnO Sustainable Coatings Against Multidrug-Resistant (MDR) Uropathogens and UreC-Positive *Proteus mirabilis*

Awad Kadim Shaalan Al-Khalidy [1], Ali Jabbar Abd Al-Hussain Alkawaz [2,*], Maryam Sabah Naser [3] and Ali Jalil Obaid [3]

[1] College of Administration and Economics, Warith Al-Anbiyaa University, Karbala 56001, Iraq; awad.ka@uowa.edu.iq
[2] Department of Biology, College of Science, University of Kerbala, Karbala 56001, Iraq
[3] Department of Applied Biotechnology, College of Biotechnology, Al-Qasim Green University, Babylon 51001, Iraq; maryam.h@biotech.uoqasim.edu.iq (M.S.N.); ali.j@biotech.uoqasim.edu.iq (A.J.O.)
* Correspondence: ali.abdulhussein@uokerbala.edu.iq; Tel.: +964-7802771914

Abstract

Introduction: Catheter-associated urinary tract infections (CAUTIs) caused by multidrug-resistant (MDR) uropathogens pose a management challenge due to bacterial biofilm formation and crystalline encrustation, especially those associated with *Proteus mirabilis*, which result in persistent infections and catheter obstructions. Current catheter surface coatings against CAUTIs target either the initial stages or later phases of such pathologies separately. **Aim**: We report the design and characterization of a novel polyfunctional coating comprised of polydopamine (PDA), genipin-crosslinked chitosan (GCS), and ZnO nanoparticles capable of blocking bacterial attachment, biofilm formation, and mineral encrustation. **Methods**: PDA-coated silicon surfaces were functionalized with genipin-crosslinked GCS/ZnO nanocomposites and studied by means of TEM, XRD, FTIR, SEM, AFM, water contact angle measurements, and zinc ion release tests. Antibacterial, antibiofilm, anti-encrustation, and hemocompatibility activities were then assessed. **Results**: ZnO nanoparticles were spherical, with an average particle size of 34.6 ± 8.2 nm and a highly crystalline hexagonal wurtzite structure. Coatings containing ZnO nanoparticles retained hydrophilic surface properties and released Zn^{2+} ions steadily. The G5 coating (containing 0.2% ZnO) demonstrated an ability to decrease bacterial adherence by >4 $\log_{10}$ CFU, lower biofilm biomass by 80–90% ($p < 0.001$), prevent mineral deposition by 67–70% caused by *Proteus mirabilis*, and keep catheter patency for 14 days. Hemolysis was within the ISO 10993-4 acceptance criteria. **Conclusions**: A rationally designed combination of PDA, genipin-crosslinked GCS, and ZnO nanoparticles provided a multifunctional coating with potent antibacterial, antibiofilm, anti-encrustation, and initial hemocompatibility activity, serving as a proof-of-concept platform for further cytotoxicity assessment, mechanical durability studies, and preclinical evaluations prior to clinical implementation.

Keywords: biofilm inhibition; catheter-associated urinary tract infection (CAUTI); chitosan–ZnO nanocomposite coating; multidrug-resistant (MDR) uropathogens; *Proteus mirabilis* encrustation

Check for updates

Academic Editor: Nurettin Sahiner

Received: 23 June 2026
Revised: 7 August 2026
Accepted: 17 August 2026
Published: 1 September 2026

Copyright: © 2026 by the authors. Licensee MDPI, Basel, Switzerland. This article is an open access article distributed under the terms and conditions of the Creative Commons Attribution (CC BY) license.

1. Introduction

Catheter-associated UTIs are among the most common healthcare-acquired infections globally, causing significant morbidity, hospital stays, and healthcare costs, especially for

extended catheterization [1–3]. The risk of developing bacteriuria is directly correlated with catheter use time, with a daily incidence of 3–10% that leads to infections in most chronically catheterized individuals [4]. Biofilm formation on the catheter surface provides bacteria with protection from antibiotics and immune responses, increasing the risk of reinfection [5]. Uropathogenic organisms, especially *P. mirabilis*, are difficult to treat because their urease activity produces ammonia, thereby alkalizing the urine and promoting the crystallization of apatite and struvite, which can lead to premature catheter obstruction and failure [6,7].

Although many antimicrobial coatings for catheters have been synthesized, most focus on bacterial adherence and do not address interrelated processes such as MDR biofilm formation, urine alkalinization, crystallization, and catheter obstruction [8,9]. The use of chitosan in coating materials is justified by its antimicrobial, antibiofilm, and biocompatible properties; nonetheless, its poor water stability limits its use. Crosslinking of chitosan with genipin ensures increased stability and durability while maintaining biocompatibility [10,11]. ZnO-NPs enhance the antimicrobial potential of chitosan through the controlled release of zinc ions and the production of ROS [12,13].

Because blood exposure can occur during catheterization, another criterion coatings must meet is hemocompatibility. Thus, the developed coatings must meet the existing hemocompatibility requirements. However, it must be understood that hemocompatibility alone does not confer full biocompatibility, and in the future, will have to be combined with mammalian cell toxicity tests [14,15]. To facilitate better binding between the coating and the silicone material, a widely used substance is polydopamine (PDA).

Recently, several multifunctional catheter coatings with antimicrobial properties have been developed, including infection-responsive coatings [15], mussel-inspired dopamine-based surface systems [16], mussel-inspired nanocomposite catheter coatings [17], silver-based hydrogel coatings [18], and ZnO-based composite catheters [19]. Still, these approaches mostly consider the individual functions—antimicrobial action, antibiofilm efficiency, drug delivery system, lubricity, infection-responsive release—but a simultaneous comprehensive analysis of all mentioned functions as well as catheter encrustation, Zn^{2+} ions release kinetics, reactive oxygen species production, and hemocompatibility against MDR clinical uropathogens in one multifunctional system is lacking. Also, while the applications of PDA, chitosan, and ZnO for biomedical surfaces have been reported individually, the rational development of stable, multifunctional coatings that simultaneously control different stages of the CAUTI infection process still requires further research. Nevertheless, the aforementioned studies provide the scientific basis for the multifunctional approach used in the present study.

Hence, the current study demonstrates a hierarchically designed multifunctional coating wherein polydopamine (PDA) acts as an adhesive primer to the silicone surface, genipin provides structural stability to the chitosan-based coating material in the aqueous medium of the urine, and ZnO nanoparticles contribute with concentration-dependent antibacterial activity through zinc ion release and the generation of reactive oxygen species. The performance of the coating was systematically assessed against multidrug-resistant pathogens isolated from patients with UTIs, namely ureC-positive *P. mirabilis*, in human urine.

The novelty of this research lies not in the individual use of PDA, chitosan, genipin, or ZnO; all of these materials have already been used in biomedical surface engineering. The novelty lies in the logical combination of these materials into a single multifunctional coating and a comprehensive assessment of its effects across the consecutive phases of CAUTI pathogenesis, including bacterial attachment, the formation of MDR biofilms, urinary alkalinization via urease enzymes, crystalline mineral deposition, and catheter occlusion. A comparative analysis of recent urinary catheter coatings is given in Table 1.

Table 1. Concise comparison of representative recent urinary-catheter coatings and the present multifunctional coating.

Study	Coating System	Main Evaluation	Anti-Encrustation	MDR Clinical Isolates	Key Distinction
Ivanova et al., 2021 [8]	pSBMA/Polymyxin B nanoparticles	Antibacterial, antibiofilm	No	No	Antimicrobial peptide-based coating; no Zn^{2+} release or encrustation model.
Miao et al., 2023 [9]	polySBMA-TA pH-responsive hydrogel	Antibacterial, pH-responsive release	Yes	No	Smart drug-delivery hydrogel without ZnO nanocomposite evaluation.
Slate et al., 2023 [15]	Infection-responsive theranostic coating	Biofilm, blockage warning	Yes	No	Drug-release system focused on blockage detection and delay.
Puertas-Segura et al., 2024 [17]	Gelatin/Ag-Au nanoparticle coating	Antibacterial, antibiofilm	No	No	In vivo antimicrobial coating without Zn^{2+} release or ROS analysis.
Yang et al., 2024 [18]	PDA-assisted Ag hydrogel	Antibacterial, antiadhesive	No	No	Silver hydrogel emphasizing lubrication and biocompatibility.
Kim et al., 2025 [19]	ZnO-CNT incorporated catheter	Antimicrobial, antibiofilm	No	No	Bulk ZnO-CNT catheter without encrustation or hemocompatibility studies.
Present study	PDA/genipin-crosslinked chitosan/ZnO	Antibacterial, antibiofilm, Zn^{2+} release, ROS, hemocompatibility	Yes	Yes	Multifunctional platform integrating MDR evaluation, Zn^{2+} release, ROS, and dynamic anti-encrustation.

Despite recent advances, most antimicrobial coatings for urinary catheters still focus only on particular aspects of CAUTI development, such as bacteriostatic or biofilm-inhibiting properties, but fail to adequately solve the problem of complex interrelated processes starting with MDR bacterial colonization and moving further to the alkalinization of urine, crystal-forming biofilm, catheter encrustation, and obstruction [8,9]. In addition, although ZnO nanoparticles and PDA-coated chitosan surfaces are known to have impressive antimicrobial and stabilizing properties individually, combining them into a single multifunctional coating that inhibits multiple stages of CAUTI pathogenesis remains underexplored [12,18].

In translational research, commercially available antimicrobial urinary catheters, especially silver alloy or nitrofurazone-coated catheters, primarily prevent the early stages of bacterial colonization but are less effective against mature biofilms, multidrug-resistant uropathogens, urease-induced encrustation, and catheter occlusion. In contrast, the current research introduces an innovative approach to address these interconnected pathophysiological phenomena by synergistically integrating surface immobilization, controlled release of Zn^{2+} ions, antibiofilm effects, and crystallization prevention. While a direct comparison between our catheters and commercially available catheters was outside the scope of this research, currently available data indicate that the proposed multifunctional concept provides a strong basis for future comparative investigations.

Strategies for antimicrobial urinary catheter coatings that have been developed in recent years are shown in Table 1. The scope of the new multifunctional platform was compared to that of previous studies in this respect. Unlike studies that focused on antibac-

terial activity, antibiofilm properties, drug-delivery responsiveness, lubricity, or infection-responsive catheter protection in general, this study combines three aspects: PDA-based adhesion, chitosan stabilization via genipin, and ZnO-based antimicrobial activity. The coating was evaluated for its effectiveness against multidrug-resistant clinical uropathogens, Zn^{2+} ion release, reactive oxygen species production, hemocompatibility, and performance in a 14-day dynamic model of *Proteus mirabilis* encrustation and catheter obstruction.

2. Materials and Methods

2.1. Materials and Substrate Preparation

Medical-grade silicone substrates (1 × 1 cm) and sections of Foley catheters (2 cm) were used. Dopamine hydrochloride (≥98%), Tris (hydroxymethyl) aminomethane (Tris, molecular biology grade), genipin (≥98%), glacial acetic acid (ACS reagent grade), Tween® 80, nitric acid (HNO_3, analytical grade), and PBS tablets were purchased from Sigma-Aldrich (Merck, St. Louis, MO, USA). Chitosan (medium molecular weight, degree of deacetylation 85%) was purchased from Sigma-Aldrich (Merck, St. Louis, MO, USA). Zinc oxide nanoparticles (ZnO, particle size 20–50 nm, ≥99%) were provided by Merck KGaA (Darmstadt, Germany). HTCC (*N*-(2-hydroxypropyl)-3-trimethylammonium chitosan chloride) was purchased from Sigma-Aldrich (Merck, St. Louis, MO, USA). Only deionized water was used in all of the experiments.

Substrates were cleaned by sonication in 70% ethanol for 5 min, then rinsed in deionized water and dried. Activation was carried out by oxygen plasma treatment using a PDC-32G plasma cleaner (Harrick Plasma, Ithaca, NY, USA) at 100–150 W and 0.3 mbar O_2 under vacuum for 5 min. Priming layers of PDA were applied by incubating cleaned substrates in dopamine hydrochloride (2 mg/mL) in 10 mM Tris-HCl solution (pH 8.5) for 3 h at RT and in the dark, allowing dopamine polymerization and forming a poly(dopamine) (PDA) layer. Subsequently, treated substrates were rinsed and dried, yielding PDA-coated silicone (G1) [20,21].

2.2. Fabrication of Chitosan–Genipin ± ZnO Coatings

The solution of chitosan with a deacetylation degree of 85% was made in acetic acid of 1% (*v*/*v*) concentration in order to prepare the 0.75% (*w*/*v*) solution of chitosan at approximately pH 5.5. A parallel solution was prepared by mixing a 1% (*w*/*v*) HTCC solution with the chitosan solution at a 1:1 ratio. This resulted in a coating solution containing 0.5% chitosan, 0.5% HTCC, and 0.5% acetic acid [22,23].

ZnO with sizes between 20 and 50 nm was added to the polymer matrix in two different concentrations of 0.05% and 0.20% (*w*/*v* compared to the amount of polymer). Before adding the ZnO nanoparticles to the polymer mixture, they were ultrasonicated in a 70:30 (water:ethanol) mixture containing 0.1% Tween-80 for 30 min. After that, the dispersion mixture was combined with the CS–genipin composite, stirred, and ultrasonicated for 5 min to prevent nanoparticle clustering [24,25].

The characterization of ZnO nanoparticles (ZnO NPs) prior to their use in preparing the coating solution included transmission electron microscopy (TEM), dynamic light scattering (DLS), zeta potential analysis, and X-ray diffraction (XRD). The TEM analysis was carried out using a JEOL JEM-2100 transmission electron microscope (JEOL Ltd., Tokyo, Japan) operated at an acceleration voltage of 200 kV. For TEM analysis, the ZnO nanoparticles were diluted, drop-cast onto a carbon-coated copper grid, and dried. The DLS and zeta potential values of ZnO nanoparticles were measured by a Zetasizer Nano ZS (Malvern Panalytical, Malvern, UK) at 25 °C. The XRD analysis of ZnO nanoparticles was conducted using an X'Pert PRO diffractometer (Malvern Panalytical, Almelo, The Netherlands) operated at 40 kV and 30 mA using Cu Kα radiation (λ = 1.5406 Å). The XRD

patterns were taken within the 2θ range of 20–80°, with a step size of 0.02° and a scanning speed of 2° min^{-1} [26,27].

The substrates were dipped in a chitosan–ZnO solution (10–15 min) at a withdrawal speed of 5 mm min^{-1} to ensure a uniform coating thickness. After 12 h of air drying, the coatings were chemically crosslinked with genipin dissolved in fresh solutions (0.25%, *w*/*v* in 10 mM phosphate-buffered saline at pH 7.4) for 18 h at room temperature in the absence of light. After washing and drying, chitosan–genipin-based hydrolytically stable coatings were obtained. Coatings without ZnO are termed G3, while ZnO-containing coatings are termed G4 (with 0.05% ZnO) and G5 (with 0.2% ZnO) [28–30].

Before performing the biological test, all sample containers were sterilized by exposure to EtO gas at 37 °C for 12 h. After sterilization, all sample containers were handled aseptically throughout the experiment [31].

2.3. Bacterial Isolates and MDR Confirmation

The study involved five multidrug-resistant clinical uropathogens: *E. coli*, *K. pneumoniae*, *P. aeruginosa*, *S. aureus*, and *P. mirabilis.* The samples were collected from patients with urinary tract infections and stored frozen at −80 °C. Ethically approved methods were employed to process the samples. In selecting *P. mirabilis*, the decision was informed by the bacterium's high urease production and ureC-positive status [32].

The isolates were resuscitated in tryptic soy agar and then incubated overnight in tryptic soy broth (TSB). Resistance to multiple drugs was assessed according to the CLSI guidelines using the disk diffusion technique. To test resistance to multiple drugs, antibiotics from six classes were used. An isolate was said to be MDR when it showed resistance to at least one drug belonging to three or more different classes. All isolates in the present study were MDR, including ESBL-producing *E. coli*, *K. pneumoniae*, carbapenem-resistant *P. aeruginosa*, MRSA, and multidrug-resistant *P. mirabilis*. The presence of the ureC gene in *P. mirabilis* was confirmed by PCR using specific primers [33].

The presence of the ureC gene in *Proteus mirabilis* was confirmed by PCR using primers reported in earlier studies. The DNA extraction process involved boiling in TE buffer, which produced a 400-base-pair product. A urease-negative *E. coli* strain served as a negative control, while a *Proteus mirabilis* reference strain acted as the positive control [32].

2.4. Biofilm Formation and Inhibition Assays in Urine

The static biofilm studies were conducted by collecting urine from 3 to 5 healthy individuals using sterile techniques after obtaining informed consent. The urine samples were combined to reduce differences in urine composition, filtered through a 0.45 µm filter to remove particulate matter, and stored in the refrigerator until use. Within 24 h of collection, the urine had a pH of approximately 6.2 [34].

The overnight cultures of bacteria were diluted in a composite urine medium to obtain a final concentration of approximately 10^6 CFU/mL and inoculated into 24-well plates with either coated or non-coated sterile silicon samples (n = 5 per group). After a 24-h incubation period at 37 °C, the samples were washed with PBS followed by sonication with 1 mL PBS (at 40 kHz for 5 min) in order to detach the bacterial cells from the surface. Serial dilutions and plating were carried out on tryptic soy agar plates, and the bacterial counts were determined and recorded in logarithmic form, CFU/sample [35].

The biofilm biomass was determined using the crystal violet (CV) assay. Incubated and washed samples were stained with 0.1% crystal violet solution for 15 min. After the incubation period, excess dye was removed, and samples were destained with a 33% acetic acid solution. The optical density (OD590) was recorded after the stain-destaining step and corrected for sample surface area [36].

The key criteria for effectiveness in this study were changes in the number of adherent bacterial cells and biofilm biomass compared with the non-coated group. A good coating was expected to lead to a 2-$\log_{10}$ reduction in adherent bacterial CFUs, along with a decrease of $\geq$50% in biofilm biomass stained with crystal violet. Controls with sterile urine and replicate testing were used to maintain validity across all studies conducted [37].

2.5. Dynamic Encrustation Model with P. mirabilis

Catheter encrustations were studied employing a dynamic model for *Proteus mirabilis* urinary tract infections. Silicone catheter segments, 2 cm long with an internal diameter of 4 mm, were exposed to a constant urine flow rate of approximately 5 mL/h at 37 °C. To provide a continuous challenge from *P. mirabilis*, fresh urine containing about 10^5 colony-forming units per mL was used daily. Furthermore, in some cases, a semi-batch system was also used, enabling daily urine changes [38,39].

The catheters from experimental groups G0, G3, and G5, each consisting of 5 samples, were investigated for over 14 days, with assessments on day 7. Daily urine pH measurements were performed to evaluate the effects of urease-induced alkalization and biofilm formation associated with *Proteus mirabilis* infections. The patency of the catheters was recorded during the experiment. On days 7 and 14, catheters were removed, and deposit masses were measured by gravimetry. The dried samples were baked at 60 degrees Celsius for 24 h, then washed, dried, and weighed again to determine the mineral mass. SEM/EDS analysis of deposits was performed to assess the morphology and chemical composition of crystals, focusing on magnesium, phosphorus, and calcium as markers of struvite and hydroxyapatite. The locations of high pH in the biofilm were determined using the phenolphthalein staining technique. The anti-encrustation efficiency was estimated as the ratio of deposit masses across different experimental groups when the reduction was at least 60 percent [40–42].

2.6. Water Contact Angle (WCA)

Static water contact angle is the parameter used to quantify the interaction between water and a solid surface at equilibrium. This parameter plays an important role in understanding wetting phenomena and surface energies because it is the ratio of adhesion forces at the liquid–solid interface to cohesion forces within the liquid. Small contact angles indicate hydrophilicity, which allows water to spread, while high contact angles indicate hydrophobicity, preventing water from spreading. This parameter is of paramount importance in materials science, coatings, and surface treatments. The contact angle of 5 µL of distilled water was measured on surfaces G0–G5 before and after 7- and 14-day immersion in sterile urine at 37 °C [43,44].

2.7. Fourier Transform Infrared Spectroscopy (FTIR)

In the current research, infrared spectroscopy was performed on PDA-coated silicone, CS–genipin coatings (both with and without ZnO addition), and ZnO nanoparticles alone. Scans were made within the wavenumber range of 4000–400 cm^{-1} with a resolution of 4 cm^{-1}, using 32 scans per spectrum. This was conducted to reveal characteristic absorption peaks of PDA, chitosan, and the crosslinking agent genipin, as well as interactions between Zn and O atoms [45–47].

2.8. Scanning Electron Microscopy (SEM)

The surface morphological features were analyzed using a JSM-IT500 scanning electron microscope (JEOL Ltd., Tokyo, Japan) equipped with energy-dispersive X-ray spectroscopy (EDS) at an accelerating voltage of 5 kV, with gold/palladium-sputtered sample surfaces. The tests were carried out to analyze the distribution, uniformity, thickness, morphology,

post-biofilm formation, and crystallite deposition. Energy-dispersive X-ray spectroscopy (EDS) mapping was employed to verify the distribution and retention of zinc during immersion in urine [48–50].

2.9. Atomic Force Microscopy (AFM)

The surface roughness was determined using tapping-mode Atomic Force Microscopy (AFM) with a Dimension Icon atomic force microscope (Bruker, Billerica, MA, USA), scanning over a 5 μm square area. Root mean square roughness (Rq) was determined to analyze the impact of PDA coating, formation of chitosan-genipin coating, and addition of ZnO nanoparticles on the nano-topography of the samples [51].

2.10. ZnO Content and Zinc Release Kinetics

The total amount of zinc was calculated by dissolving a specific area of the coating in a 2% HNO_3 solution, and Inductively Coupled Plasma Optical Emission Spectroscopy (ICP-OES; Agilent 5110, Agilent Technologies, Santa Clara, CA, USA) was then used to analyze the resulting solution. Using these calculations, the base zinc loading ($\mu g/cm^2$) for coatings containing ZnO (ZnO) could be determined [52,53].

Zinc ion elution studies involved exposing G4 and G5 coatings to sterile human urine at 37 °C for a total volume of 5 mL. Samples were collected at 6 h, 24 h, 72 h, 7 days, and 14 days, then subjected to acidification with 2% nitric acid. This was followed by analysis using inductively coupled plasma-optical emission spectroscopy (ICP-OES). The volume of urine samples was replenished after each sample was taken to maintain sink conditions throughout the test period [48,54,55].

2.11. Zn^{2+} Release and Mechanistic Analyses

ROS production was assessed using the DCFH-DA fluorescence assay. The samples obtained from groups G0, G3, G4, and G5 were mixed with PBS containing 10 μM DCFH-DA at 37 °C for 2 h. Subsequently, fluorescence intensity was analyzed using a Synergy H1 microplate reader (Agilent Technologies, Santa Clara, CA, USA) at an excitation wavelength of 485 nm and an emission wavelength of 530 nm. RFU values were calculated per square centimeter of sample surface area [56,57].

The kinetic studies of the total release of Zn^{2+} ions were carried out using four popular mathematical models: zero-order, first-order, Higuchi, and Korsmeyer–Peppas models in order to investigate the release mechanism that dominates in the synthesized nanocomposite coating. The applicability of the models mentioned was estimated using the coefficient of determination (R^2), root mean square error (RMSE), and Akaike information criterion (AIC). Furthermore, the 95% confidence interval (95% CI) was calculated for the model parameters to assess their accuracy. The residual analysis involved plotting residuals against sampling time to assess model fit and systematic differences between the experimental and predicted data [58].

2.12. Hemocompatibility Evaluation

Blood from healthy volunteers was collected with their permission in accordance with the institution's ethics protocol. Hemocompatibility was evaluated in accordance with ISO 10993-4 using hemolysis and morphology tests. Isolation of the erythrocytes and preparation of the 2% suspension were performed. Samples belonging to G0-G5 were exposed to erythrocytes at 37 °C for 1 h. Phosphate-buffered saline and distilled water were used as negative and positive controls. The rate of hemolysis was quantified using a UV-1900i UV–Vis spectrophotometer (Shimadzu Corporation, Kyoto, Japan) at 540 nm [59,60].

After coating the surfaces, the erythrocytes were fixed with 2.5% glutaraldehyde, then dehydrated in ethanol at different concentrations. Scanning electron microscopy was used to observe the structure of the erythrocytes and assess the condition of their membranes to examine the impact of the materials being examined [61,62].

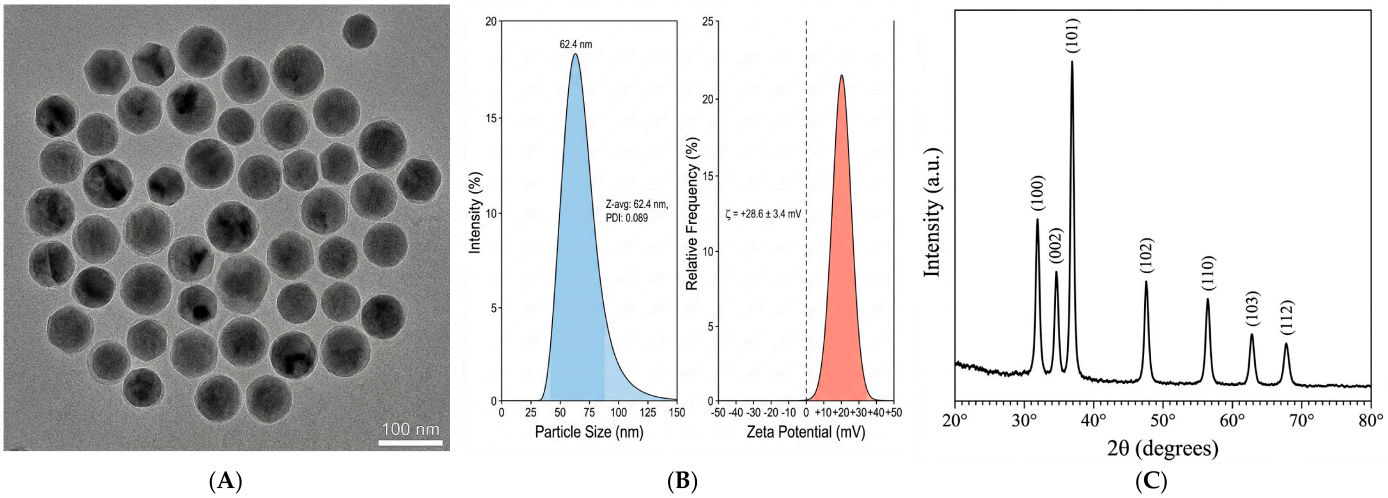
2.13. Statistical Analysis

All experimental assays used three to five independent biological replicates, as required, with values expressed as mean ± standard deviation (SD). Normality of the data was first established before any statistical test. Datasets that exhibited normal distribution were subjected to one-way ANOVA and Tukey's multiple comparisons test. When the assumptions of the parametric tests were not met, the nonparametric Kruskal–Wallis test was used. Statistical significance was set at a p value of less than 0.05. Statistical analysis was carried out using GraphPad Prism, version 9 (GraphPad Software, San Diego, CA, USA) [63].

3. Results

3.1. Physicochemical Characterization of ZnO Nanoparticles

ZnO nanoparticle characterization before the coating deposition was carried out by means of TEM, DLS, zeta potential measurements, and X-ray diffraction (XRD). According to TEM studies, the predominant shape of the nanoparticles was spherical, with the average diameter of 34.6 ± 8.2 nm. The XRD pattern (Figure 1C) had typical diffraction peaks at 2θ angles of 31.8°, 34.4°, 36.3°, 47.5°, 56.6°, 62.8°, and 67.9° for the (100), (002), (101), (102), (110), (103), and (112) crystallographic planes, respectively, of hexagonal wurtzite ZnO (JCPDS No. 36-1451). No additional peaks attributable to secondary phases were detected in the diffraction pattern, confirming the phase purity of the nanoparticles. Average crystallite size estimated by means of the Debye–Scherrer equation was 32.8 ± 2.1 nm, which correlates well with the particle diameter determined by TEM, i.e., 34.6 ± 8.2 nm. The slight difference is expected, since XRD provides information on the coherent crystalline domain size, whereas TEM characterizes the particle diameter. Therefore, good agreement between XRD and TEM indicates that the synthesized ZnO nanoparticles are highly crystallized. The main physicochemical parameters of the ZnO nanoparticles are presented in Table 2.



(**A**) (**B**) (**C**)

Figure 1. (**A**) TEM micrograph of ZnO nanoparticles showing particle morphology and size distribution. (**B**) Hydrodynamic size distribution and zeta potential of ZnO nanoparticles determined by DLS analysis. (**C**) XRD pattern of ZnO nanoparticles.

Table 2. Physicochemical properties of ZnO nanoparticles.

Parameter	Value	Characterization Method
Particle size (nm)	34.6 ± 8.2	TEM
Crystallite size (nm)	32.8 ± 2.1	XRD (Debye–Scherrer equation)
Hydrodynamic diameter (nm)	62.4 ± 11.7	DLS
Zeta potential (mV)	+28.6 ± 3.4	Zeta potential analysis
Particle morphology	Predominantly spherical to slightly hexagonal	TEM
Crystal structure	Hexagonal wurtzite	XRD
Major diffraction peaks (2θ, °)	31.8, 34.4, 36.3, 47.5, 56.6, 62.8, 67.9	XRD
Phase purity	No detectable impurity phases	XRD
Colloidal stability	Moderate stability	Zeta potential analysis

3.2. Reactive Oxygen Species Generation

The addition of ZnO significantly increased ROS production, as illustrated in Table 3 and Figure 2. Groups G0 and G3 showed almost identical fluorescence, but the addition of ZnO greatly increased ROS production. The amount of ROS was 258 ± 18 RFU in G4 and 451 ± 25 RFU in G5, corresponding to approximately 2.6- and 4.5-fold higher ROS levels than those of the control group ($p < 0.001$). ZnO incorporation significantly increased ROS generation, with G5 showing the highest fluorescence intensity across all groups ($p < 0.001$).

Table 3. Reactive oxygen species (ROS) generation by different coating formulations.

Group	Relative ROS (RFU)
G0	100 ± 8
G3	112 ± 10
G4	258 ± 18
G5	451 ± 25

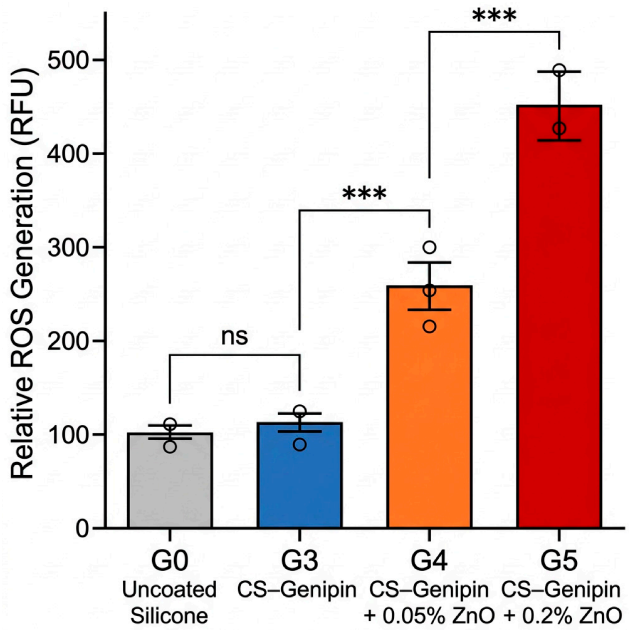


Figure 2. Reactive oxygen species (ROS) generation by the coated silicone surfaces was measured using the DCFH-DA assay. Values represent mean ± SD ($n = 3$). *** $p < 0.001$; ns, not significant.

The concentration-dependent ROS generation behavior of the coatings is illustrated in Figure 2.

The increase in ROS generation with increasing ZnO content indicates that the oxidation process is strongly correlated with the number of nanoparticles in the coating matrix. Much higher fluorescence intensity was observed in G5 than in G4, and the data confirm that a higher zinc oxide concentration increases the coating surface's oxidation capacity. The correlation between this effect and the antibacterial action of zinc oxide coatings confirms that ROS is one of the main mechanisms involved in bacterial growth inhibition. Together with the continuous release of ions, as confirmed in the current study, these data indicate that the coating under study exerts antimicrobial action via oxidative and ionic mechanisms rather than a single mechanism.

3.3. Coating Formation and Characterization

CS–genipin ± ZnO coatings could be uniformly deposited onto the surface of the silicone substrates. It was noted that a polydopamine (PDA) primer coating followed by genipin crosslinking enabled the formation of stable, adherent films with no peeling observed. The introduction of ZnO into the coating composition had no adverse effect, except for an increase in surface roughness at a ZnO concentration of 0.2%.

Measurement of the water contact angle showed an effective improvement in surface hydrophilicity (Figure 3). While for non-coated silicone, the contact angle value was approximately 98°, for substrates with the PDA coating, it dropped to around 72°, and for substrates with the CS–genipin coating, it dropped to about 45–50°. At the same time, ZnO did not affect the initial surface wetting properties. After two weeks of incubation in artificial urine, the contact angles remained below 60° under all studied conditions, indicating the preservation of hydrophilic properties.

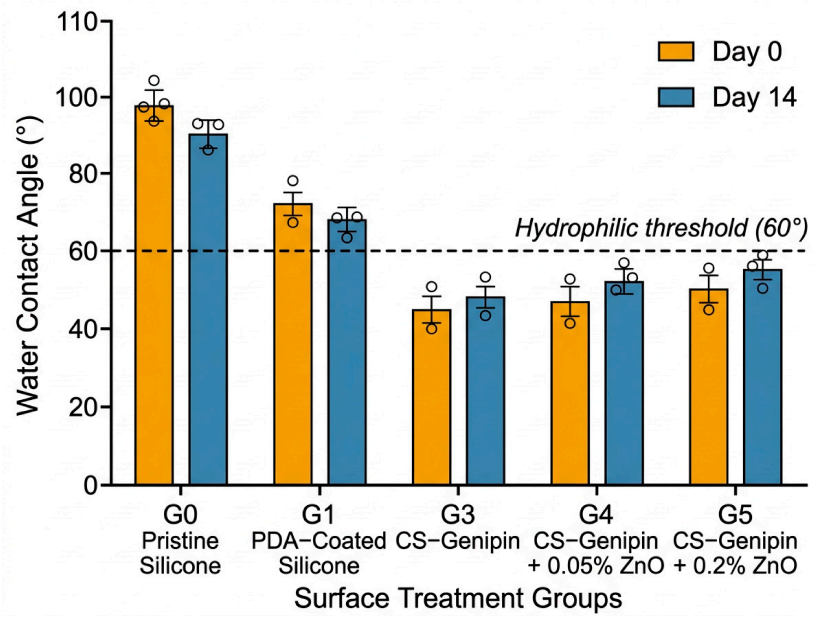


Figure 3. Water contact angle of uncoated and coated silicone surfaces at baseline and after 14 days of immersion in human urine (37 °C). Values represent mean ± SD (n = 3).

The observed absorption peaks were consistent with the expected chemical structures of PDA, genipin-crosslinked chitosan, and ZnO nanoparticles, and the absence of additional absorption peaks indicated no undesirable side reactions or impurities.

The ATR-FTIR spectra (Figure 4) provide evidence of the stepwise formation of a multifunctional coating. A broad band at approximately 3300 cm^{-1} is related to overlapping

O–H and N–H stretching vibrations due to hydroxyl and amino groups in PDA and chitosan. The peak at 1720 cm^{-1} represents the presence of C=O stretching vibrations belonging to ester and carbonyl groups due to the crosslinking reaction of genipin. The peak at 1637 cm^{-1} is assigned to the amide I band (stretching C=O) and the C=N stretch (Schiff base), indicating successful covalent crosslinking between genipin and the amino groups of chitosan. The peak at 1155 cm^{-1} represents the asymmetric stretching vibration of the glycosidic C–O–C bridge within the chitosan chain. The peaks at 1076 cm^{-1} and 1028 cm^{-1} correspond to C–O stretching vibrations in the polysaccharide backbone, indicating that chitosan's molecular structure is preserved after crosslinking. Finally, the peak at 430 cm^{-1} corresponds to Zn–O lattice-stretching vibrations in ZnO nanoparticles, confirming their presence in the resulting coating.

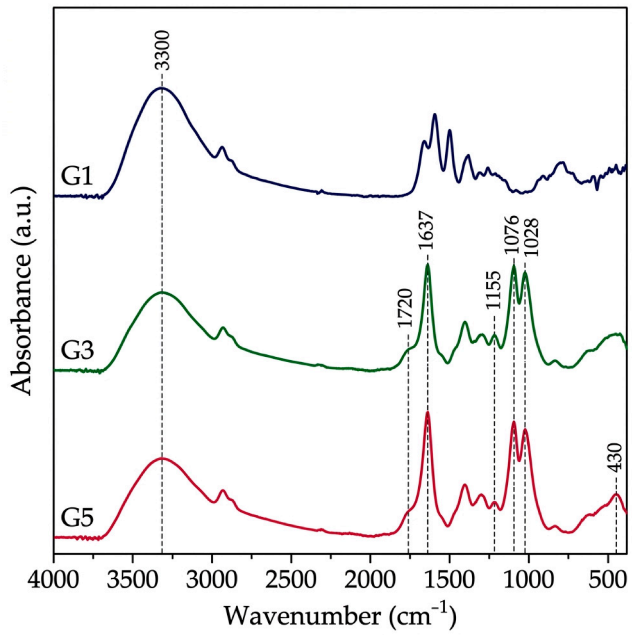


Figure 4. ATR-FTIR spectra of the uncoated and coated silicone surfaces showing characteristic functional groups of PDA, CS–genipin, and ZnO-containing coatings.

The study, carried out using a scanning electron microscope (SEM), revealed a homogeneous surface coating and a uniform distribution of nanoparticles (Figure 5A). The quantitative analysis of the SEM images (n = 186 particles) revealed an average nanoparticle size of 35.2 ± 8.1 nm (median = 34.8 nm), which was similar to the particle size determined by TEM: 34.6 ± 8.2 nm. The coating that did not have any ZnO showed some wrinkling and porosity, while the ZnO-containing coating revealed uniformly distributed nanoparticles with some small aggregates without any sign of phase segregation. Moreover, the distribution of zinc was confirmed using EDS mapping.

From the AFM analysis (as shown in Figure 5B), a gradual increase in surface roughness was observed after the addition of PDA, followed by the addition of the CS–genipin coating and the further addition of ZnO. RMS roughness increased from about 4 nm for the bare silicone surface to 40–60 nm for the ZnO-containing coatings. This is consistent with nanoparticle loading and was confirmed by the scanning electron microscopy (SEM) results.

The coatings showed good adherence and resistance. It was found that there was no peel-off of the coating in the tape adhesion test and that the genipin crosslinking successfully prevented dissolution when the tape was exposed to urine for an extended period. The CS–genipin coatings were better at maintaining their structure over the duration of the experiment than the non-crosslinked chitosan coatings. Ethylene oxide sterilization also had no negative effect on the coatings' properties and appearance.

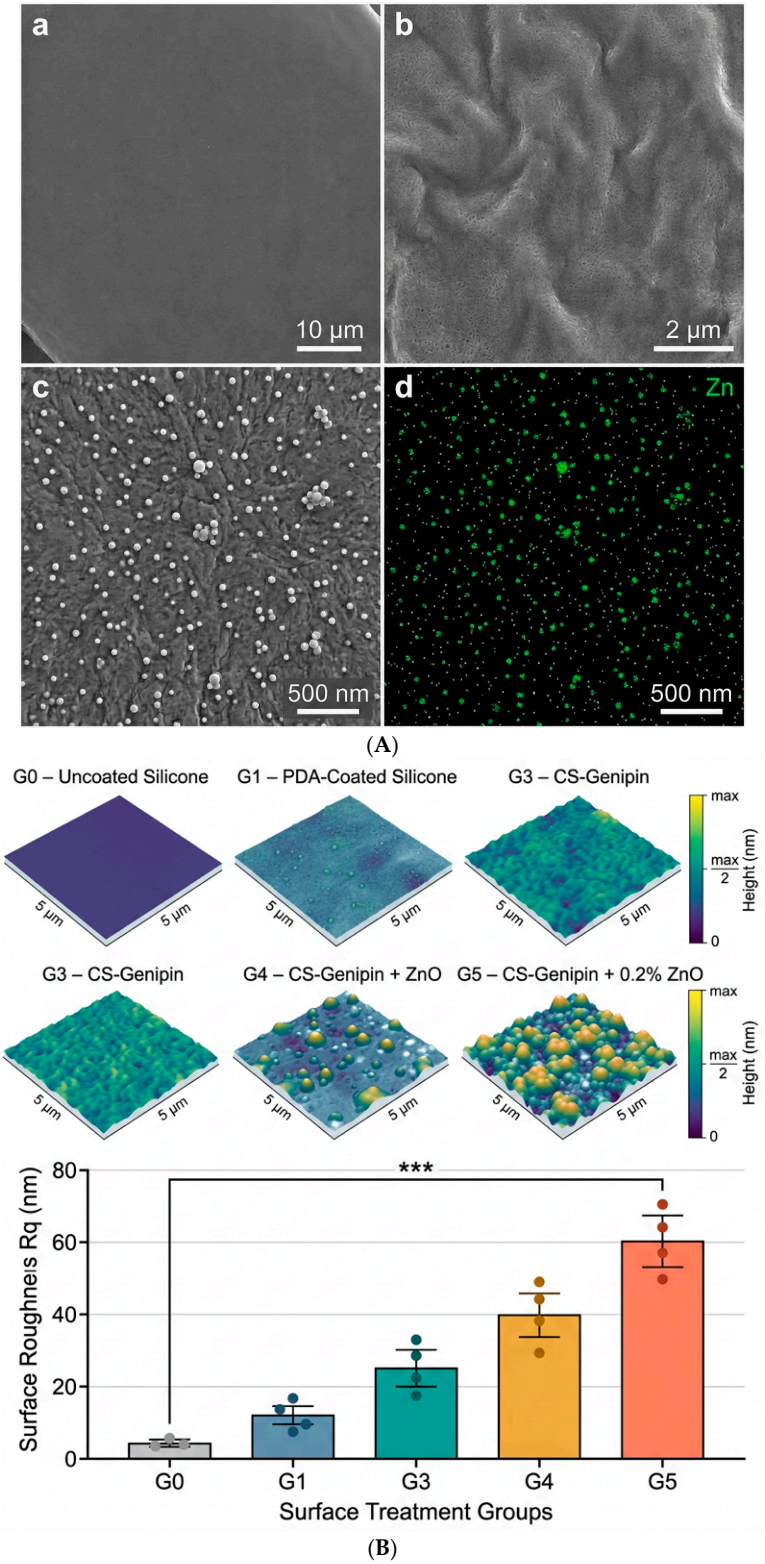


Figure 5. (**A**) Representative SEM micrographs and EDS elemental mapping of the uncoated and coated silicone surfaces. (**a**) Uncoated silicone substrate. (**b**) Genipin-crosslinked chitosan coating. (**c**) CS–genipin coating containing ZnO nanoparticles. (**d**) Corresponding Zn elemental EDS mapping showing the homogeneous distribution of ZnO nanoparticles. Quantitative SEM image analysis (n = 186 particles) yielded a mean particle size of 35.2 ± 8.1 nm (median = 34.8 nm). (**B**) Surface roughness (Rq) of the uncoated and coated silicone surfaces measured by AFM. Values represent mean ± SD. *** $p < 0.001$ indicates a statistically significant difference.

While prolonged aging studies lasting months could not be performed in the current study, several pieces of evidence support the initial stability of the obtained coating under physiological conditions. No observable signs of coating delamination or deterioration, such as surface cracks, were observed during the 14 days of continuous immersion in urine or during the dynamic encrustation test. Hydrophilicity of the coating, maintenance of its morphological properties, detection of zinc by EDS, and preservation of antimicrobial and anti-encrustation activities suggest that the PDA-mediated crosslinked polymeric coating is stable during prolonged immersion in an aqueous environment. However, further studies to assess long-term stability will include accelerated aging, repeated sterilization cycles, cyclic mechanical loading, and storage stability testing.

3.4. Antibacterial and Anti-Biofilm Efficacy

The antimicrobial and anti-biofilm activities of these coating formulations were assessed for multidrug-resistant uropathogens grown in human urine samples for 24 h of incubation at 37 °C. While the chitosan–genipin coatings demonstrated reduced bacterial attachment and biofilm formation, the ZnO coatings exhibited the greatest inhibitory activity (Figure 6).

It can be seen from Figure 6A that strong biofilms developed on plain silicone surfaces, achieving 7.5 $\log_{10}$ CFU of *E. coli* and 7.0 $\log_{10}$ CFU of *P. mirabilis* bacteria. Isolation of bacteria on PDA had little influence on bacterial adhesion. Conversely, the CS–genipin coatings reduced bacterial adhesion by nearly 1.5 $\log_{10}$ CFU for both bacterial types, resulting in an inhibition rate close to 97%.

The CS–genipin coating with 0.2% ZnO (G5) exhibited the strongest antibacterial activity. On the G5-coated surfaces, adherent bacterial counts decreased to 3.5 $\log_{10}$ CFU/sample for *E. coli* and 3.0 $\log_{10}$ CFU/sample for *P. mirabilis*, representing reductions of more than 4 $\log_{10}$ CFU relative to the uncoated controls ($p < 0.001$). The coating with 0.05% ZnO (G4) resulted in an intermediate level of reduction. Generally, the G5 coating showed the best antibacterial effect, while the G4 coating showed the second-best reduction due to its ZnO content.

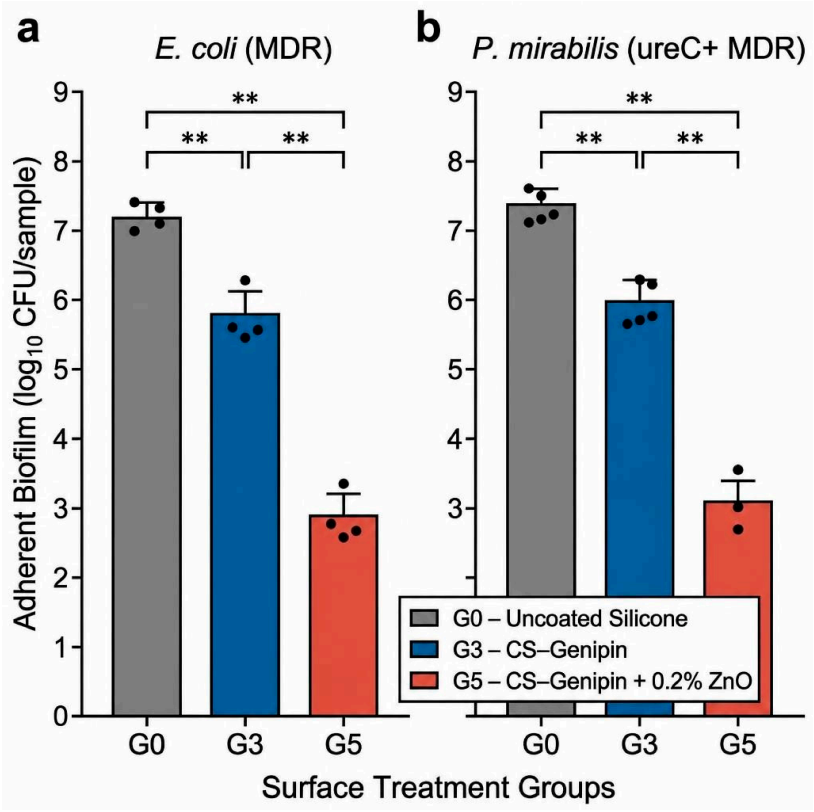
Similar results were obtained for *K. pneumoniae*, *P. aeruginosa*, and *S. aureus*. Combinations of chitosan and genipin coatings reduced biofilm growth by 1–2 $\log_{10}$ CFU. However, for the ZnO coatings, the reduction rate exceeded 3 $\log_{10}$ CFU for all tested bacteria. This enhanced antibacterial activity is likely associated with the sustained Zn^{2+} release and concentration-dependent ROS generation provided by the incorporated ZnO nanoparticles.

Crystal violet staining experiments supported the above observations. OD590 for uncoated silicone ranged from 1.0 to 1.5. In contrast, the chitosan and genipin coatings decreased the biofilm biomass by 50–70%, while the additional presence of ZnO resulted in an 80–90% reduction and near-baseline OD590 readings.

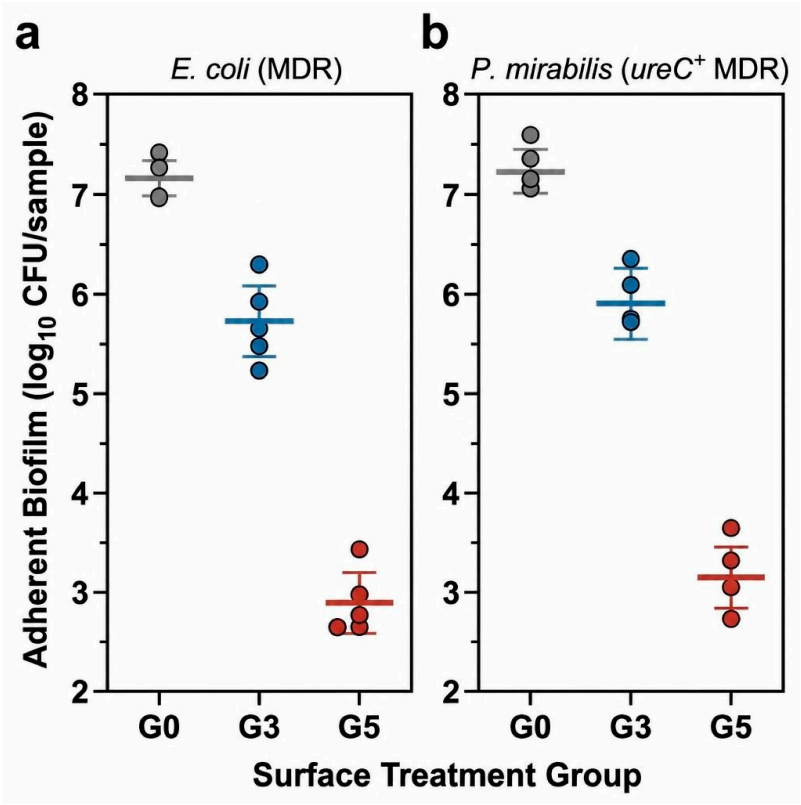
Consistent results were shown by visual and scanning electron microscopy analyses. The surface of the uncoated silicone was colonized by tightly packed bacterial colonies in the ECM matrix, whereas ZnO coatings contained only isolated bacterial cells, suggesting compromised membrane integrity.

Overall, the new coatings surpassed existing performance standards, resulting in more than 2 $\log_{10}$ CFU reductions and considerable inhibition of biofilm biomass. The presence of ZnO (ZnO) significantly improved antimicrobial activity across the entire spectrum against the MDR strain set.

ANOVA statistical tests confirmed significant variations between experimental groups ($p < 0.0001$). Specifically, CS–genipin and CS–genipin + ZnO were found to be superior to the control in reducing bacterial adhesion. On the other hand, the coating with 0.2% ZnO proved more effective than that with 0.05%.



(**A**)



(**B**)

Figure 6. (**A**) Adherent biofilm counts ($\log_{10}$ CFU/sample) of (**a**) MDR *Escherichia coli* and (**b**) ureC-positive MDR *Proteus mirabilis* recovered from coated and uncoated silicone surfaces after 24 h incubation in human urine. Values represent mean ± SD (n = 5). (**B**) Individual replicate values of adherent bacterial counts recovered from the coated and uncoated silicone surfaces. Horizontal lines indicate mean ± SD (n = 5). ** $p < 0.01$ indicates a statistically significant difference.

3.5. Inhibition of Encrustation and Blockage in the P. mirabilis Urine Model

The effectiveness of the coating in reducing encrustations was assessed based on an experiment conducted in a dynamic urine model using bacteria (*Proteus mirabilis*). The results showed that uncoated catheters formed a crystalline biofilm within several hours, accompanied by increased bacterial growth, alkalization of the solution, and eventual blockage. Struvite and hydroxyapatite were found in considerable quantities, resulting in complete obstruction of the catheters within 4–5 days.

On the other hand, the CS–genipin + ZnO (G5) coatings were highly effective at preventing encrustation and keeping catheters open during the experiment. The pH of the solution increased more slowly than in the control catheters and stabilized at 7.2–7.5 for two days, then reached 8.0 after 7 days (compared with more than 8.5 in the uncoated system). It was shown that during a 14-day test period, no ZnO-coated catheters had full obstruction, whereas control catheters were completely blocked by day 7 ($p < 0.01$).

Mineral accumulation on the uncoated catheters was approximately 60 mg, whereas the G5-coated catheters exhibited a residual deposit mass of approximately 18–20 mg. Accordingly, the G5 coating reduced mineral deposition by approximately 67–70% relative to the uncoated control ($p < 0.01$) (Figure 7).

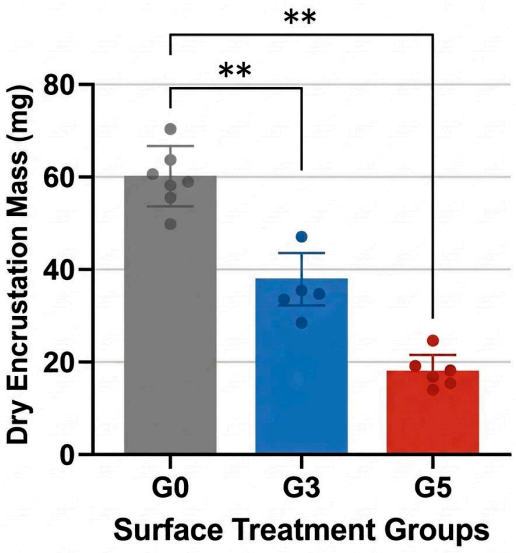


Figure 7. Encrustation mass of catheter segments after 14 days in the *Proteus mirabilis* urine infection model. Values represent mean ± SD ($n = 5$). ** $p < 0.01$.

A decline in encrustation mass of more than 60% was achieved in both groups and was statistically significant ($p < 0.001$), with a larger effect seen in G5. Replicate results are shown in Table 4 and illustrated graphically in Figure 8.

Table 4. Individual encrustation mass measurements after 14 days in the *P. mirabilis* model.

Replicate	G0 (mg)	G5 (mg)
1	56	18
2	63	20
3	59	19
4	62	17
5	60	21
Mean ± SD	60.0 ± 2.7	19.0 ± 1.6

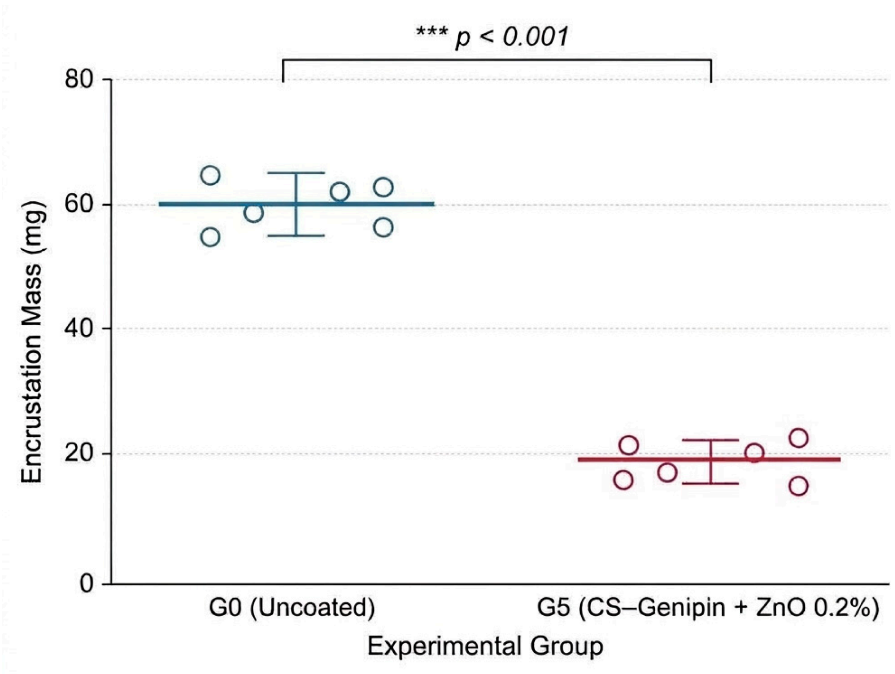


Figure 8. Individual encrustation measurements of catheter segments after 14 days in the *Proteus mirabilis* urine infection model. Horizontal bars indicate mean ± SD (n = 5).

The distribution of individual encrustation values is shown in Figure 8.

The SEM and EDS analyses supported these findings. Untreated catheters had considerable amounts of biofilm in the form of crystals, with struvite and hydroxyapatite significantly enriched in Mg, P, and Ca. In contrast, ZnO-coated surfaces exhibited small, minimally sized crystals with large areas lacking biofilm, indicating inhibition of bacterial adhesion and crystal formation.

CS–genipin coatings without ZnO were effective at reducing encrustations and deposit formation; however, their effectiveness was lower than that of coatings containing ZnO. This highlights the importance of the continuous release of antibacterial Zn^{2+} ions in blocking crystal formation by inhibiting urease activity.

The integrity of the coatings was preserved during all experiments. The ZnO coatings had a contact angle less than 55°, a surface zinc content, and no degradation upon extended exposure to alkaline urine and bacterial strains.

In conclusion, the CS–genipin + ZnO coating is highly effective at preventing biofilm crystallization, resulting in a 70% reduction in encrustation. Furthermore, it delays urine alkalinization and prevents catheter obstruction for at least 2 weeks, providing significant protection against complications associated with *Proteus mirabilis* infections.

3.6. Hemolysis and Hemocompatibility Results

All tested coatings had low hemolytic potential, with hemolysis levels ranging from 1.8 ± 0.4% (G3) to 3.4 ± 0.5% (G5), and none exceeding 5%, as defined by ISO 10993-4 (Figure 9). No statistically significant differences were observed between the zinc oxide coatings and the other experimental groups ($p > 0.05$). Using scanning electron microscopy (SEM), intact erythrocyte membranes were observed in all samples of coated materials, while the positive control exhibited ruptured membranes. Overall, the results show that the created coatings are hemocompatible under the present experimental conditions. The hemolysis values and ISO classifications for all experimental groups are listed in Table 5.

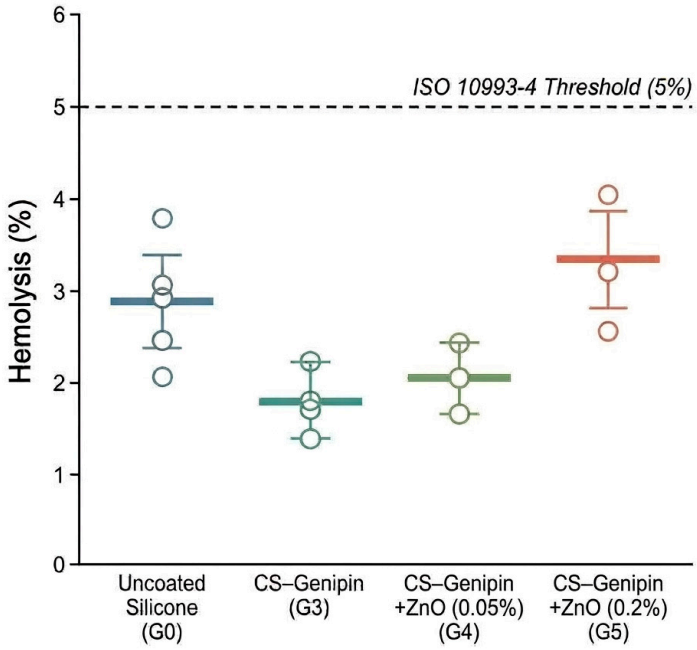


Figure 9. Hemolysis of coated and uncoated catheter surfaces following incubation with human erythrocytes. The dashed line indicates the ISO 10993-4 hemocompatibility threshold.

Table 5. Hemocompatibility assessment of the coated and uncoated silicone surfaces.

Group	Hemolysis (%)	ISO Classification
G0	2.9 ± 0.5	Non-Hemolytic
G3	1.8 ± 0.4	Non-Hemolytic
G4	2.1 ± 0.3	Non-Hemolytic
G5	3.4 ± 0.5	Non-Hemolytic

3.7. Zinc Release Profile

Zinc release studies were performed to evaluate the sustained-release behavior of the ZnO-containing coatings (Figure 10).

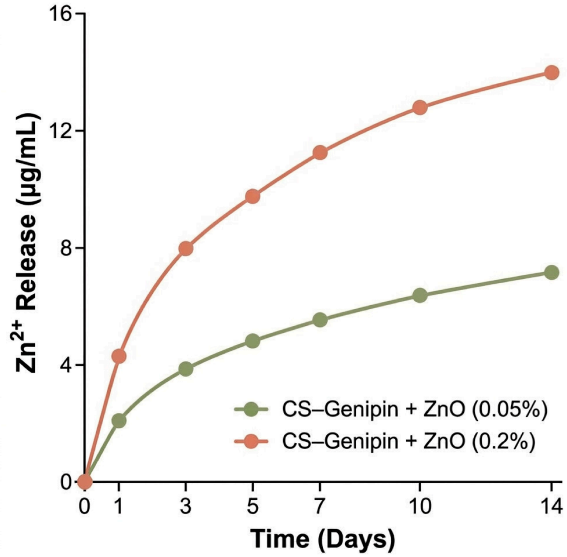


Figure 10. Cumulative Zn^{2+} release from the CS–genipin coatings containing 0.05% and 0.2% ZnO nanoparticles during immersion in human urine at 37 °C over 14 days. Values represent the mean of three independent samples.

The introduction of ZnO into both of the materials caused a gradual release of Zn^{2+} ions during 14 days. Particularly, the level of G5 increased from 2.1 µg/mL at 6 h to 14.0 µg/mL on day 14, whereas G4 increased from 0.8 µg/mL to 7.1 µg/mL (Figure 10). It was observed that there were no signs of a burst-release effect in either material. It has been shown that the genipin crosslinked scaffold has the potential to control the diffusion rate of Zn^{2+} ions.

Statistical evaluation of four kinetic models was carried out using the coefficient of determination (R^2), root mean square error (RMSE), Akaike information criterion (AIC), and 95% confidence intervals (95% CI) for the fitted parameters (Table 6). Furthermore, a residual analysis was conducted to assess the adequacy of the model fit (Figure 11).

Table 6. Statistical comparison of Zn^{2+} release kinetic models.

Model	Parameter(s)	R^2	RMSE	AIC	95% CI
Zero-order	k_0 = 4.68 µg·cm^{-2}·day^{-1}	0.946	2.91	31.8	4.11–5.25
First-order	k_1 = 0.182 day^{-1}	0.962	2.21	27.6	0.161–0.203
Higuchi	kH = 18.74 µg·cm^{-2}·day$^{-½}$	0.992	0.71	15.4	17.82–19.66
Korsmeyer–Peppas	kKP = 14.9, n = 0.46	0.988	0.95	18.1	k: 14.1–15.7; n: 0.42–0.50

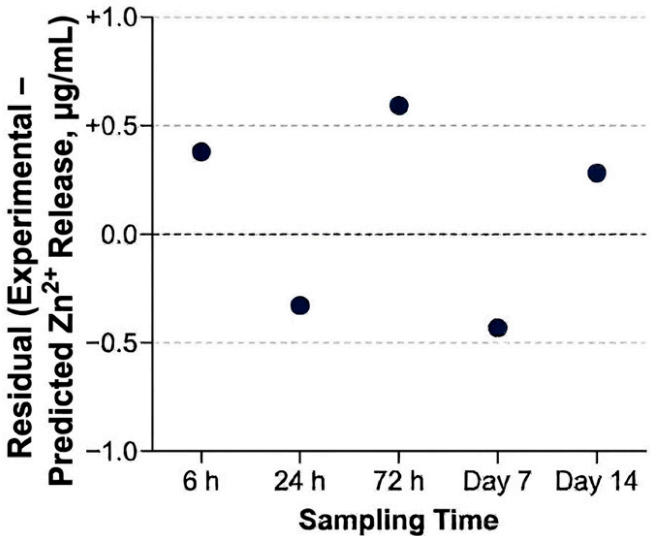


Figure 11. Residual plot of the best-fitting Higuchi model showing the distribution of residuals across the experimental sampling times.

Of the tested models, the Higuchi model showed the best overall fit, with the highest coefficient of determination (R^2 = 0.992), the lowest RMSE (0.71), and the lowest AIC (15.4). Furthermore, the narrow 95% confidence interval for the fitted model parameter indicates high precision in its estimate. As can be seen from the residual plot, the residuals were randomly distributed around zero, indicating adequate model fit and the absence of bias.

Taken together, the statistical data presented above show that the Higuchi model adequately describes the release pattern of Zn^{2+} from the developed coating of PDA/genipin-crosslinked chitosan/ZnO. Diffusion control is likely to prevail in this case.

3.8. Minimum Inhibitory Concentration (MIC) and Minimum Bactericidal Concentration (MBC) of ZnO Nanoparticles

The antibacterial effect of ZnO nanoparticles on MDR *E. coli* and ureC-positive MDR *P. mirabilis* followed a dose-dependent relationship, as presented in Table 7. The MIC and MBC values for MDR *E. coli* and ureC-positive MDR *P. mirabilis* were 4 and 8 µg/mL

and 6 and 12 µg/mL, respectively. Consistent with the sustained zinc-release behavior, the G5 coating delivered incrementally higher zinc-ion levels that reached or exceeded the MIC values toward the latter stages of the release phase. This continuous release of ions, along with the dose-dependent production of ROS, explains the notable decrease in bacterial adherence, biofilm formation, and catheter encrustation. Overall, the findings show a complementary antimicrobial mechanism that includes chitosan-mediated contact inhibition and a sustained Zn^{2+} antimicrobial effect.

Table 7. Minimum inhibitory concentration (MIC) and minimum bactericidal concentration (MBC) of ZnO nanoparticles against representative MDR uropathogens.

Bacterial Isolate	MIC (µg/mL)	MBC (µg/mL)
MDR *E. coli*	4	8
MDR *P. mirabilis* (ureC+)	6	12

4. Discussion

4.1. Physicochemical Characteristics of ZnO Nanoparticles

Physicochemical characterization revealed that the embedded ZnO nanoparticles possess properties favorable for biomedical surface modification. The results obtained from TEM, DLS, zeta potential, and XRD analyses reveal the presence of nanometer-sized particles with moderate colloidal stability and high crystallinity. It is important to note here that the physicochemical properties of nanoparticles are found to affect the Zn^{2+} ion release rate, production of ROS, antimicrobial effects, and interaction of nanoparticles with the surface. Therefore, the improved biological performance of the coatings is possibly due to the well-defined physicochemical properties of the embedded ZnO nanoparticles [64–66].

4.2. Antibacterial and Anti-Biofilm Performance

The CS–genipin–ZnO coating exhibited significant antibacterial and antibiofilm properties against MDR uropathogens, demonstrating reductions of >3–4 $\log_{10}$ CFU in bacterial adhesion and biofilm formation. These findings are consistent with previous studies that have described the antibacterial properties of ZnO-based coatings against uropathogens and on medical devices with biofilms. Significantly, the CS–genipin–ZnO coating maintained its antibacterial activity despite being stable in the presence of urine over an extended period [67–69].

The increased antimicrobial efficacy observed in this study is consistent with the concentration-dependent formation of reactive oxygen species (ROS) and the continuous release of Zn^{2+} ions, both of which were determined in this study. The results are consistent with the established antimicrobial mechanisms of chitosan and zinc oxide (ZnO) nanoparticles from previous research. It is believed that chitosan acts by blocking bacterial adhesion through electrostatic interactions between chitosan and the negatively charged bacterial envelope. Meanwhile, the mechanism of ZnO nanoparticles involves ROS formation and the continuous release of Zn^{2+} ions. However, since the mechanisms were not studied in this experiment, they can only be considered plausible biological mechanisms [70–72].

The considerable decrease in bacterial load (>3 $\log_{10}$ CFU) for all MDR uropathogens tested aligns with the suggested complementary actions of the coating against bacteria. The positively charged chitosan matrix is most likely responsible for the decreased bacterial adhesion. In contrast, the continuous release of Zn^{2+} ions, along with the formation of reactive oxygen species by ZnO nanoparticles, which increases with increasing concentration, probably disrupts bacterial cell membrane metabolism.

There is synergy between the polymer matrix and nanoparticles, leading to greater effectiveness of the ZnO-coated substrates than the chitosan–genipin coating. This is also

consistent with reports from previous studies in which the presence of nanoparticles within chitosan-based metal oxides increased their effectiveness in inhibiting biofilm formation and their antibacterial activity [66,73,74].

4.3. Minimum Inhibitory and Bactericidal Activity of ZnO Nanoparticles

The MIC and MBC values provide further evidence of the coating's antibacterial potential. Zinc oxide nanoparticles exhibited fairly low MIC/MBC values against the multiresistant strains of *Escherichia coli* (MIC/MBC 4/8 μg/mL) and ureC-positive, multiresistant *Proteus mirabilis* (MIC/MBC 6/12 μg/mL). The continuous release of Zn^{2+} ions from the G5 coating reached or exceeded these MIC/MBC levels, suggesting that the reduced adhesion, biofilm formation, and encrustation of catheters by bacteria were attributable to sustained Zn^{2+} ion release along with the production of reactive oxygen species and membrane damage. These observations are consistent with previous studies implicating the antimicrobial properties of ZnO nanoparticles in Zn^{2+} ion release and membrane damage. The slightly higher MIC/MBC values for *P. mirabilis* compared with *E. coli* may be related to species-specific features of cell envelopes [64,65].

The agreement between the Zn^{2+} release profile and the measured MIC/MBC values suggests that the coating maintained biologically relevant antimicrobial concentrations throughout the experimental period, thereby supporting its sustained antibacterial activity.

4.4. Hemocompatibility Assessment

All coating compositions complied with the hemocompatibility requirements set by ISO 10993-4, as the hemolysis percentage did not exceed the critical value of 5%. In addition, SEM observations showed that erythrocyte morphology was maintained after contact with the coated materials, indicating negligible acute blood cell damage. The findings are consistent with earlier studies on the blood compatibility of chitosan and ZnO biomaterials [59,75,76].

4.5. Anti-Encrustation Effects

One of the key observations from this study was the significant anti-encrustation activity exhibited by the ZnO-based coating against *P. mirabilis*. It inhibited urine alkalinization, prevented mineral deposition by about 70%, and maintained catheter patency for 14 days. In contrast to other previously developed antimicrobial catheter coatings that focused on preventing bacterial colonization, the current multifunctional coating not only restricted the formation of crystalline biofilms, but also prevented catheter obstruction [77–79].

There are several complementary modes of action for the anti-entrapment properties noted: the first being that Zn^{2+} can interfere with the urease reaction, followed by the suppression of mineral formation and the prevention of biofilm maturation. The significant reduction in bacterial load, coupled with the presence of the hydrophilic chitosan substrate, may have decreased crystal formation, leading to less mineral deposition on the catheter surface [80,81].

In general, the study results demonstrate that the multicomponent film acts as an anti-encrustation coating by preventing bacterial colonization, sustaining the release of Zn^{2+}, delaying urine alkalinization, and decreasing mineral deposition [82,83].

4.6. Controlled Zinc Release Behavior and Kinetic Interpretation

Zn^{2+} sustained release becomes one of the key features of the proposed coating. Since there is no burst-release stage and the agreement with the Higuchi kinetic equation is quite good, zinc ion release from the genipin crosslinked polymer can be assumed to occur mainly via diffusion. This would allow the antimicrobial effect to be maintained while

minimizing excessive zinc release. Diffusion-controlled release has been reported for other crosslinked chitosan-based antimicrobial systems [84–86].

4.7. Biocompatibility Considerations

However, the biocompatibility of the elements used in the coating has already been well-studied and shows satisfactory results. In addition, in this study, Zn^{2+} concentrations remained within the range where cytotoxic effects were not expected. However, it cannot be concluded that these elements provide complete biological safety. A thorough biocompatibility test in accordance with ISO 10993-5, followed by preclinical testing, is still necessary before the clinical application of this new coating [87–89].

4.8. Comparison to Other Coatings and Clinical Context

In contrast to traditional antibiotic-coated, silver-coated, hydrogel, and other monofunctionalized urine catheters, the current system incorporates multiple functionalities, including contact-active antibacterial properties, Zn^{2+} delivery, anti-biofilm properties, and protection against crystallization. The multi-functionality approach aims to address various phases of the CAUTI mechanism rather than focusing solely on bacterial adhesion. Therefore, the new catheter coating has the potential to prevent the development of biofilms and encrustation by MDR bacteria, but further investigations comparing the novel catheter system with commercially available catheters are required [90–93].

4.9. Innovation and Novelty

The key strength of the current investigation lies in the rational combination of PDA-enabled surface adhesion, genipin-crosslinked chitosan, and zinc oxide nanoparticles into a unified multifunctional coating system. While introducing a novel material does not seem to be an issue here, what is really unique about the current research is the development of a coating that incorporates several already existing biomaterials to perform several functions at once: prevent bacterial adhesion and biofilm formation, demonstrate antimicrobial properties, and avoid crystalline encrustation and catheter occlusion.

4.10. Limitations

There are various limitations of this study that need to be noted before interpreting the results. Although the hemocompatibility of the coating was analyzed in accordance with ISO 10993-4, the mammalian cell cytotoxicity test according to ISO 10993-5 was not included in this proof-of-concept experiment. Therefore, the presented results are functional performance and preliminary blood-compatibility test results, rather than a complete biological safety assessment. Future experiments will need to include standardized cytotoxicity assays for the relevant urothelial and fibroblast cell lines and the following in vivo preclinical evaluation.

Although the coating showed good adhesion, retained its structure after ethylene oxide sterilization, and maintained stability during long-term urine immersion, durability tests were not performed. For future experiments, it is necessary to conduct clinically relevant mechanical tests including abrasion resistance, cyclic bending, friction during insertion, repeated mechanical stress, accelerated aging, storage stability, and resistance to repeated sterilizations.

The final limitation is that even though all the antibacterial, antibiofilm, ROS generation, Zn^{2+} release, and anti-encrustation properties of the coating indicate a multi-mechanism antimicrobial effect, the quantitative contribution of each mechanism to the total effect was not measured. Future experiments will help deepen our understanding of the coating's mechanism of action.

4.11. Potential Clinical Impact

Upon successful implementation in clinical settings, this multifunctional coating could help reduce the risk of CAUTIs and catheter encrustation by simultaneously inhibiting MDR biofilms and *Proteus mirabilis* encrustation. Given the ease with which such coatings can be manufactured from readily available biomaterials, this technology may be scalable. It can help prolong the functional lifespan of catheters and reduce catheter changeovers and antibiotic use, leading to potential savings for patients and the healthcare system overall. However, all of the above-mentioned advantages need to be validated in future clinical studies [8,94–96].

The present work presents initial data on blood compatibility tested according to the ISO 10993-4 hemocompatibility assay. Low hemolysis and the absence of any changes in erythrocyte shape indicate negligible acute injury to blood cells during the experiment. However, it must be kept in mind that hemocompatibility is only one aspect of biological compatibility and cannot serve as an indicator of overall biocompatibility.

4.12. Future Directions

In future studies, the long-term stability, durability, and biological activity of the coating need to be tested under clinical conditions. Future studies need to include animal experiments, scalability and sterilization of the coating, and a comparison of the developed coating with commercial antimicrobial catheters. Moreover, the use of this coating method in other urinary devices, such as ureteral stents and nephrostomy tubes, could provide additional applications for this technique. Finally, the use of additional antimicrobial or anti-inflammatory agents could improve the coating's effectiveness.

5. Conclusions

The current research outlines an intelligent design and provides a complete characterization of a multifunctional coating for the surface modification of a urinary catheter, including the development of a polydopamine (PDA)-based, genipin-crosslinked chitosan/ZnO nanocomposite coating. This coating shows excellent physicochemical stability, a constant release of zinc ions, the generation of reactive oxygen species (ROS) that depends on their concentration, and initial hemocompatibility under the defined experimental conditions. In terms of functionality, this coating efficiently prevents adhesion and biofilm formation by multidrug-resistant (MDR) pathogens and *Proteus mirabilis*-associated crystallization and maintains the catheter's patency in a 14-day dynamic urine model. Thus, these findings show that a combination of the PDA-based surface attachment, genipin-crosslinked chitosan, and ZnO nanoparticles in a single multifunctional coating system can exert simultaneous effects across several steps of CAUTI pathogenesis. Further studies are needed on cytotoxicity, durability, and preclinical testing before any clinical use; however, the developed coating is a prospective platform for next-generation antimicrobial urinary catheters.

Author Contributions: Conceptualization, A.J.A.A.-H.A.; methodology, A.J.A.A.-H.A. and M.S.N.; validation, M.S.N., A.K.S.A.-K. and A.J.O.; formal analysis, A.J.A.A.-H.A. and A.K.S.A.-K.; investigation, A.J.A.A.-H.A. and M.S.N.; data curation, M.S.N.; writing—original draft preparation, A.J.A.A.-H.A.; writing—review and editing, A.J.A.A.-H.A., M.S.N. and A.K.S.A.-K.; visualization, A.K.S.A.-K.; supervision, A.J.O.; project administration, A.J.O. All authors have read and agreed to the published version of the manuscript.

Funding: This research received no external funding.

Institutional Review Board Statement: The study was conducted in accordance with the ethical principles of the Declaration of Helsinki (1975, as revised in 2013) and was approved by the Research

Ethics Committee of the College of Science, University of Kerbala, Iraq (Approval No. 0037CSE; Approval Date: 13 May 2026).

Informed Consent Statement: Written informed consent was obtained from all healthy volunteers who donated urine and blood samples for this study. Clinical bacterial isolates were anonymized before being made available to the investigators, and no personally identifiable information was collected or accessed.

Data Availability Statement: The datasets generated and analyzed during the current study are available from the corresponding author upon reasonable request. All experimental procedures, raw data, and analytical methods supporting the findings of this study can be provided for verification and further research purposes.

Acknowledgments: The authors would like to express their sincere appreciation to Warith Al-Anbiyaa University, the University of Kerbala, and Al-Qasim Green University for providing the academic environment and institutional support that facilitated this research. The authors also thank the laboratory staff and all individuals who contributed to the successful completion of this study. During the preparation of this manuscript, the authors used ChatGPT (GPT-4o, OpenAI) for the purposes of language editing, improving clarity, grammar, readability, and presentation of the manuscript. The authors have reviewed and edited the output and take full responsibility for the content of this publication.

Conflicts of Interest: The authors declare no conflicts of interest.

References

1. Nappi, F.; Avtaar Singh, S.S. Prevalence of healthcare-associated infections in developing and developed countries: A systematic review. *BMC Infect. Dis.* **2026**, *26*, 1135. [CrossRef] [PubMed]
2. Werneburg, G.T. Catheter-associated urinary tract infections: Current challenges and future prospects. *Res. Rep. Urol.* **2022**, *14*, 109–133. [CrossRef] [PubMed]
3. Patel, P.K.; Advani, S.D.; Kofman, A.D.; Lo, E.; Maragakis, L.L.; Pegues, D.A.; Pettis, A.M.; Saint, S.; Trautner, B.; Yokoe, D.S.; et al. Strategies to prevent catheter-associated urinary tract infections in acute-care hospitals: 2022 update. *Infect. Control Hosp. Epidemiol.* **2023**, *44*, 1209–1231. [CrossRef] [PubMed]
4. Hou, D.; Jia, Y.; Han, A.; Hu, Q.; Li, J.; Liang, W. Effect of urinary catheter removal at different times after caesarean section: A systematic review and network meta-analysis. *Eur. J. Obstet. Gynecol. Reprod. Biol.* **2023**, *280*, 160–167. [CrossRef] [PubMed]
5. Tegegne, D.T.; Abbott, I.J.; Poźniak, B. Catheter-associated urinary tract infections: Understanding the interplay between bacterial biofilm and antimicrobial resistance. *Int. J. Mol. Sci.* **2025**, *26*, 9193. [CrossRef] [PubMed]
6. Fitzgerald, M.J.; Pearson, M.M.; Mobley, H.L.T. *Proteus mirabilis* UreR coordinates cellular functions required for urease activity. *J. Bacteriol.* **2024**, *206*, e0003124. [CrossRef] [PubMed]
7. Wong, E.S.; Young, C.; Yuan, Y.; Abdel-Fattah, M. Do catheter washouts reduce catheter-associated urinary tract infections and catheter blockage compared to standard care in adults living with long-term catheters? *Can. Urol. Assoc. J.* **2026**, *20*, E275–E283. [CrossRef] [PubMed]
8. Ivanova, A.; Ivanova, K.; Tzanov, T. Simultaneous Ultrasound-Assisted Hybrid Polyzwitterion/Antimicrobial Peptide Nanoparticles Synthesis and Deposition on Silicone Urinary Catheters for Prevention of Biofilm-Associated Infections. *Nanomaterials* **2021**, *11*, 3143. [CrossRef] [PubMed]
9. Miao, J.; Wu, X.; Fang, Y.; Zeng, M.; Huang, Z.; Ouyang, M.; Wang, R. Multifunctional hydrogel coatings with high antimicrobial loading efficiency and pH-responsive properties for urinary catheter applications. *J. Mater. Chem. B* **2023**, *11*, 3373–3386. [CrossRef] [PubMed]
10. Silvestre, J.; de Baynast, H.; Michaud, P. Optimization of chitosan adhesive properties by means of genipin crosslinking. *J. Appl. Polym. Sci.* **2024**, *100*, 828–844. [CrossRef]
11. Shi, B.; Xie, S.; Huang, D.; Wang, Y. Fully bio-based grease-resistant composite coating: Chitosan–genipin–microfibrillated cellulose for sustainable paper food packaging. *Int. J. Biol. Macromol.* **2025**, *311*, 143660. [CrossRef] [PubMed]
12. Ahamad Khan, M.; Lone, S.A.; Shahid, M.; Zeyad, M.T. Phytogenically synthesized ZnO (ZnO-NPs) potentially inhibit bacterial pathogens: In vitro studies. *Toxics* **2023**, *11*, 452. [CrossRef] [PubMed]
13. Soliman, M.; Lee, B.; Ozcan, A.; Rawal, T.B. Engineered ZnO-based nanotherapeutics boost systemic antibacterial efficacy against phloem-restricted diseases. *Environ. Sci. Nano* **2022**, *9*, 2869–2886. [CrossRef]

14. Zawidlak-Węgrzyńska, B.; Rydz, J.; Musioł, M.; Radziwon-Balicka, A. Polymer–drug antithrombogenic and hemocompatible coatings as surface modifications. *Pharmaceutics* **2024**, *16*, 432. [CrossRef] [PubMed]
15. Slate, A.J.; Clarke, O.E.; Kerio, M.; Nzakizwanayo, J.; Patel, B.A.; Jones, B.V. Infection responsive coatings to reduce biofilm formation and encrustation of urinary catheters. *J. Appl. Microbiol.* **2023**, *134*, lxad121. [CrossRef] [PubMed]
16. Li, X.; Zhang, Y.; Li, G.; Zhao, X.; Wu, Y. Mussel-inspired epoxy–dopamine polymer as a surface primer: Effect of thermal annealing treatment on enhanced adhesion performance under dry and hot/wet conditions. *Polymer* **2022**, *245*, 124693. [CrossRef]
17. Puertas-Segura, A.; Ivanova, K.; Ivanova, A.; Ivanov, I.; Todorova, K.; Dimitrov, P.; Ciardelli, G.; Tzanov, T. Mussel-Inspired Sonochemical Nanocomposite Coating on Catheters for Prevention of Urinary Infections. *ACS Appl. Mater. Interfaces* **2024**, *16*, 34656–34668. [CrossRef] [PubMed]
18. Yang, H.; Chen, Y.; Cai, Y.; Li, J.; Qiu, L.; Wang, Y.; Li, Y.; Qu, D.; Wang, R.; Zhao, Q. A feasible strategy of Ag nanoparticles-sodium alginate-polyacrylamide-polyvinyl alcohol hydrogel coatings for preventing catheter-associated urinary tract infections. *Prog. Org. Coat.* **2024**, *196*, 108706. [CrossRef]
19. Kim, S.H.; Kim, D.Y.; Park, J.S.; Park, M.; Park, M.C. Antimicrobial and Antibiofilm Activities of Urinary Catheter Incorporated with ZnO-Carbon Nanotube. *ACS Appl. Bio Mater.* **2025**, *8*, 1397–1405. [CrossRef] [PubMed]
20. Yu, P.; Pan, X.; Chen, M.; Ma, J.; Xu, B.; Zhao, Y. Ultrasound-assisted enzymatic extraction of soluble dietary fiber from *Hericium erinaceus* and its in vitro lipid-lowering effect. *Food Chem. X* **2024**, *23*, 101657. [CrossRef] [PubMed]
21. Pittiu, A.; Pannuzzo, M.; Casula, L.; Pireddu, R. Production of liposomes by microfluidics: The impact of post-manufacturing dilution on drug encapsulation and lipid loss. *Int. J. Pharm.* **2024**, *664*, 124641. [CrossRef] [PubMed]
22. Cano-Vicent, A.; Tuñón-Molina, A.; Martí, M. Biocompatible chitosan films containing acetic acid manifest potent antiviral activity against enveloped and non-enveloped viruses. *Int. J. Mol. Sci.* **2023**, *24*, 12028. [CrossRef] [PubMed]
23. Corrêa-Filho, L.C.; dos Santos Junior, J.R. Chitosan-based nanocomposite films with carnauba wax, rosin resin, and ZnO. *Food Res. Int.* **2024**, *188*, 114475. [CrossRef] [PubMed]
24. Hammani, S.; Daikhi, S.; Bechelany, M.; Barhoum, A. Role of ZnO nanoparticle loading in modifying the morphological, optical, and thermal properties of immiscible polymer (PMMA/PEG) blends. *Materials* **2022**, *15*, 8453. [CrossRef] [PubMed]
25. Erdoğdu, B.S.; Özgün, M.İ.; Madenci, E.; Sayınbatur, M.A. Production and characterization of phyto-mediated ZnO nanoparticle-reinforced PMMA-based photopolymer resins on DLP-based 3D printers. *Polymers* **2026**, *18*, 1229. [CrossRef] [PubMed]
26. Solomon, J.; Palanisamy, S.; Ravichandran, A. Characterization and investigation of biofabricated ZnO nanoparticles using *Caulerpa sertularioides* for antioxidant and antibacterial purposes. *Inorg. Chem.* **2024**, *165*, 112549. [CrossRef]
27. González-Fernández, J.V.; Pinzón-Moreno, D.D.; Neciosup-Puican, A.A.; Carranza-Oropeza, M.V. Green method, optical and structural characterization of ZnO nanoparticles synthesized using leaves extract of *Moringa oleifera*. *J. Renew. Mater.* **2022**, *10*, 833–847. [CrossRef]
28. Shigrekar, M.; Amdoskar, V. A review on recent progress and techniques used for fabricating superhydrophobic coatings derived from biobased materials. *RSC Adv.* **2024**, *14*, 32668–32699. [CrossRef] [PubMed]
29. Krishna, M.S.; Singh, S.; Batool, M.; Fahmy, H.M. A review on 2D-ZnO nanostructure-based biosensors: From materials to devices. *Mater. Adv.* **2023**, *4*, 320–354. [CrossRef]
30. Abraham, J.; Bhasker, S.P.; Samuel, S. Sustainable polymer nanocomposites for water purification. In *Materials for a Sustainable Future*; Taylor & Francis Group: Abingdon, UK, 2025. [CrossRef]
31. de Sousa Iwamoto, L.A.; Duailibi, M.T.; Iwamoto, G.Y.; de Oliveira, D.C.; Duailibi, S.E. Evaluation of ethylene oxide, gamma radiation, dry heat, and autoclave sterilization processes on extracellular matrix of biomaterial dental scaffolds. *Sci. Rep.* **2022**, *12*, 4299. [CrossRef] [PubMed]
32. Jawad, M.M.; Fayidh, M.A.; Obaid, A.S. *ureC* gene detection of *Proteus mirabilis* isolated and identified from patients with urinary tract infection. *Microbes Infect.* **2025**, *6*, 6689–6698. [CrossRef]
33. Silva, C.P.; Silva, C.L.; Haq, I.U.; Magalhães, P.P.; Farias, L.d.M.; dos Santos, V.L. Phenotypic and genotypic antimicrobial resistance profiles of Gram-positive cocci and non-fermenting Gram-negative rods. *Sci. Rep.* **2026**, *16*, 22245. [CrossRef] [PubMed]
34. Hadpech, S.; Peerapen, P.; Chaiyarit, S. Urinary proteins from stone formers promote calcium oxalate crystallization, growth, and aggregation via oxidative modifications. *J. Adv. Res.* **2025**, *81*, 125–141. [CrossRef] [PubMed]
35. Parnell, L.K.S.; Luke, N.; Mathur, M.; Festa, R.A.; Haley, E.; Wang, J.; Jiang, Y.; Anderson, L.; Baunoch, D. Elevated urinary tract infection biomarkers in symptomatic patients with urine microbial densities of 10,000 CFU/mL indicate a lower threshold for diagnosing urinary tract infections. *Diagnostics* **2023**, *13*, 2688. [CrossRef] [PubMed]
36. Jeong, S.Y.; Lee, J.W.; Kim, E.J.; Lee, C.W. Comparison of crystal violet staining, microscopy with image analysis, and quantitative PCR to examine biofilm dynamics. *FEMS Microbiol. Lett.* **2025**, *372*, fnae115. [CrossRef] [PubMed]
37. Sikosana, M.; Ruland, A.; Werner, C. Combining microscopy assays of bacteria–surface interactions to better evaluate antimicrobial polymer coatings. *Appl. Environ. Microbiol.* **2022**, *88*, e0224121. [CrossRef] [PubMed]
38. Miao, J.; Chai, H.; Niu, L.; Ouyang, M. A stable dual-functional superhydrophobic coating to inhibit *Proteus mirabilis* colonization, migration, and encrustation formation for urinary catheter applications. *J. Mater. Chem. B* **2025**, *13*, 511–523. [CrossRef] [PubMed]

39. Zhang, L. Antimicrobial Surfaces for Urinary Catheters: The Effect of Poly(glycerol Sebacate Citrate) Composition on Degradation, Encrustation and Related Performance. Ph.D. Thesis, University of Cambridge, Cambridge, UK, 2024.
40. Yang, Y.; Jia, Y.; Zhang, J.; Wang, H. A bridge-like copolymer for surface functionalization of ureteral stents with enhanced lubrication, antibacterial, and antiencrustation performances. *ACS Appl. Mater. Interfaces* **2025**, *17*, 55932–55947. [CrossRef] [PubMed]
41. Veletic, M.; Apu, E.H.; Simic, M.; Bergsland, J. Implants with sensing capabilities. *Chem. Rev.* **2022**, *122*, 16329–16363. [CrossRef] [PubMed]
42. Alkawaz, A.J.A.A.-H.; Naser, M.S.; Obaid, A.J. Biogenic TiO_2–ZnO Nanocoatings: A Sustainable Strategy for Visible-Light Self-Sterilizing Surfaces in Healthcare. *Micro* **2025**, *5*, 45. [CrossRef]
43. Zhang, J.; Xu, B.; Zhang, P.; Cai, M.; Li, B. Effects of surface roughness on wettability and surface energy of coal. *Front. Earth Sci.* **2023**, *10*, 1054896. [CrossRef]
44. Razavifar, M.; Abdi, A.; Nikooee, E.; Aghili, O.; Riazi, M. Quantifying the impact of surface roughness on contact angle dynamics under varying conditions. *Sci. Rep.* **2025**, *15*, 16611. [CrossRef] [PubMed]
45. Lin, Y.; Wu, D.; Xu, X.; Zhao, G.; Shi, B.; Wang, Y. Bio-derived active packaging: Genipin-cross-linked chitosan/cellulose nanocrystal films embedded with lemongrass essential oil for extended post-harvest fruit life. *BioResources* **2026**, *21*, 520. [CrossRef]
46. Ameer, Z.J.; Hussain, M.S.; Hussain, Z.S. Preparation and characterisation of chitosan/genipin biopolymers for tissue engineering applications. *J. Achiev. Mater. Manuf. Eng.* **2025**, *131*, 59–67. [CrossRef]
47. Agha, H.M.; Abdulhameed, A.S.; Jawad, A.H.; Khadiran, T.; Alothman, Z.A.; Wilson, L.D. Facile synthesis of crosslinked chitosan–genipin/algae composite adsorbent for cationic methyl violet dye removal: Robust modeling of adsorption using the Box–Behnken design. *J. Inorg. Organomet. Polym. Mater.* **2025**, *35*, 1084–1099. [CrossRef]
48. Awonusi, B.O.; Li, H.; Yin, Z.; Zhao, J. Surface modification of Zn–Cu alloy with heparin nanoparticles for urinary implant applications. *ACS Appl. Bio Mater.* **2024**, *7*, 1748–1762. [CrossRef] [PubMed]
49. Wang, H.; Luo, C.; Chen, W.; Wang, W.; Chen, Y. Ultrasonically synthesized Cu/Ag/Zn nanocomposite coatings for antibacterial and antibiofilm applications in urological devices. *Ultrasonics* **2025**, *123*, 107674. [CrossRef] [PubMed]
50. Won, D.S.; Lee, H.; Park, Y.; Chae, M.; Kim, Y.; Lim, B.; Kang, M.; Ok, M.; Jung, H.; Park, J. Dual-layer nanoengineered urinary catheters for enhanced antimicrobial efficacy and reduced cytotoxicity. *Adv. Healthc. Mater.* **2024**, *13*, e2401700. [CrossRef] [PubMed]
51. He, Y.; Yan, Y.; Geng, Y. Morphology measurements by AFM tapping without causing surface damage: A phase shift characterization. *Ultramicroscopy* **2023**, *254*, 113832. [CrossRef] [PubMed]
52. Al Timimi, Z.; Gide, B.; Tamimi, Z.J.M. Bioactive polymeric nanocoatings based on 4-nicotinamido-4-oxo-2-butenoic acid for enhanced corrosion resistance and biocompatibility of implantable 316L stainless steel. *J. Bio Tribo Corros.* **2026**, *12*, 90. [CrossRef]
53. Ayu, M.; Siriphannon, P.; Monvisade, P. Enhanced photocatalytic and biological properties of cellulose cotton fabric coated with carboxyethyl chitosan/ZnO bionanocomposite. *Fibers Polym.* **2025**, *26*, 3855–3869. [CrossRef]
54. Roy, P.; Saha, R.; Pawlik, J.; Samol, Z.; Dziadek, M.; Cholewa-Kowalska, K.; Chakraborty, J. Cobalt containing antimicrobial bioactive glass coated urinary catheter towards management of catheter associated urinary tract infection (CAUTI): Significant in vitro characterizations. *Ceram. Int.* **2024**, *50*, 11625–11638. [CrossRef]
55. Singh, S.; Goel, I.; Rana, A.; Gul, A. IGFBP3 repression driven by inflammation links air pollution to placental and developmental defects. *EMBO Mol. Med.* **2026**, *18*, 1648–1678. [CrossRef] [PubMed]
56. Ruijter, N.; van der Zee, M.; Katsumiti, A.; Boyles, M.; Cassee, F.R.; Braakhuis, H. Improving the dichloro-dihydro-fluorescein assay for assessment of intracellular reactive oxygen species formation by nanomaterials. *NanoImpact* **2024**, *35*, 100521. [CrossRef] [PubMed]
57. Pasciu, V.; Nieddu, M.; Sotgiu, F.D.; Baralla, E.; Berlinguer, F. An overview of assay methods for quantifying reactive oxygen species and enzymatic antioxidants in erythrocytes and spermatozoa of small domestic ruminants. *Animals* **2023**, *13*, 2300. [CrossRef] [PubMed]
58. Sihag, S.; Pal, A.; Sahewalla, S.; Saharan, V. Synthesis and characterization of Zn-bionanocrystals: Revealing pH-dependent release dynamics of encapsulated Zn^{2+} ions for sustainable applications using biopolymeric systems. *Next Nanotechnol.* **2025**, *8*, 100226. [CrossRef]
59. Moyo, M.T.G.; Adali, T.; Edebal, O.H. ISO 10993-4 compliant hemocompatibility evaluation of gellan gum hybrid hydrogels for biomedical applications. *Gels* **2024**, *10*, 824. [CrossRef] [PubMed]
60. Jitpibull, J.; Ratanavaraporn, J. Silk fibroin in medicine: A review of ISO 10993 biocompatibility, preclinical evidence, and clinical perspectives. *Adv. Ther.* **2026**, *9*, e00483. [CrossRef]
61. Loyola-Leyva, A.; Alcántara-Quintana, L.E. In vitro effect of high glucose concentrations on erythrocyte morphology assessed by scanning electron microscopy. *Micron* **2022**, *155*, 103179. [CrossRef] [PubMed]

62. Lopes, C.S.; Pronto-Laborinho, A.C.; Conceição, V.A.; Freitas, T.; Matias, G.L.; Gromicho, M.; Santos, N.C.; de Carvalho, M.; Carvalho, F.A. Erythrocyte surface properties and stiffness predict survival and functional decline in amyotrophic lateral sclerosis patients. *Clin. Transl. Med.* **2024**, *50*, 558–571. [CrossRef] [PubMed]
63. Juarros Basterretxea, J.; Aonso Diego, G. Post hoc tests in one-way ANOVA: The case for normal distribution. *Methodology* **2024**, *20*, 84–99. [CrossRef]
64. Mandal, A.K.; Katuwal, S.; Tettey, F.; Gupta, A.; Bhattarai, S. Current research on ZnO: Synthesis, characterization, and biomedical applications. *Nanomaterials* **2022**, *12*, 3066. [CrossRef] [PubMed]
65. Islam, F.; Shohag, S.; Uddin, M.J.; Islam, M.R.; Nafady, M.H. Exploring the journey of ZnO toward biomedical applications. *Materials* **2022**, *15*, 2160. [CrossRef] [PubMed]
66. Herin, R.F.; Judit, A.S.S.; Sebastiammal, S. Functionalized ZnO nanoparticles and biopolymer-coated ZnO nanoparticles for drug delivery and biomedical applications: A review. *Regen. Med.* **2025**, *11*, 165–189. [CrossRef]
67. Kumar, G.V.; Bajaber, M.A.; Mani, A.K.; Jeyanthi, V.; Velusamy, P.; Gopinath, S.C.B. Gentamicin-loaded chitosan nanocoating on polyurethane prostatic stents to combat biofilm formation and urogenital device-associated infections. *Biotechnol. Bioeng.* **2025**, *73*, 1404–1414. [CrossRef] [PubMed]
68. Jampilek, J.; Kralova, K. Advances in nanostructures for antimicrobial therapy. *Materials* **2022**, *15*, 2388. [CrossRef] [PubMed]
69. Nabawy, A. Engineered Polymer-Based Nanomaterials for the Treatment of Biofilm-Associated Infections. Ph.D. Thesis, University of Massachusetts, Amherst, MA, USA, 2024.
70. Lan, W.; Zhao, J.; Sun, Y.; Liu, J.; Xie, J. Chitosan-grafted phenolic acid copolymers against *Shewanella putrefaciens* by disrupting cell membrane permeability. *World J. Microbiol. Biotechnol.* **2022**, *38*, 73. [CrossRef] [PubMed]
71. Panigrahi, L.L.; Shekhar, S.; Sahoo, B.; Arakha, M. Adsorption of antimicrobial peptide onto chitosan-coated iron oxide nanoparticles fosters oxidative stress-triggered bacterial cell death. *RSC Adv.* **2023**, *13*, 25497–25507. [CrossRef] [PubMed]
72. Huang, Z.J.; Ye, M.N.; Peng, X.H.; Gui, P.; Cheng, F. Thiolated chitosan hydrogel combining nitric oxide and silver nanoparticles for effective treatment of diabetic wound healing. *Int. J. Biol. Macromol.* **2025**, *311*, 143730. [CrossRef] [PubMed]
73. Abdullah, J.A.A.; Jiménez-Rosado, M.; Guerrero, A. Biopolymer-based films reinforced with green synthesized ZnO. *Polymers* **2022**, *14*, 5202. [CrossRef] [PubMed]
74. Rohani, R.; Dzulkharnien, N.S.F. Green approaches, potentials, and applications of ZnO in surface coatings and films. *Bioinorg. Chem. Appl.* **2022**, *2022*, 3077747. [CrossRef] [PubMed]
75. Szymanski, L.; Golaszewska, K.; Wiatrowska, A. ISO 10993 biological evaluation of novel hemostatic powder 4SEAL®. *Biomater. Res.* **2022**, *26*, 12. [CrossRef] [PubMed]
76. Harun, N.H.; Mydin, R.B.S.M.N.; Noordin, S.S.; Sreekantan, S. Hemocompatibility profiles of LLDPE/TiO_2/ZnO nanocomposites for biomedical applications according to ISO 10993-4 and ASTM F756-00 guidelines. *BioNanoScience* **2023**, *13*, 2195–2204. [CrossRef]
77. Puspasari, V.; Ridhova, A.; Hermawan, A.; Amal, M.I. ZnO-based antimicrobial coatings for biomedical applications. *Bioprocess. Biosyst. Eng.* **2022**, *45*, 1421–1445. [CrossRef] [PubMed]
78. Kianpour, A.H.; Ahmadi-Hamedani, M.; Alamdari, S. Facile preparation of hydrophobic coatings using modified ZnO/silica composite nanoparticles. *Silicon* **2024**, *16*, 6155–6164. [CrossRef] [PubMed]
79. Mustafa, A.; Khan, I.; Chattha, M.U.; Hanif, S.; Sial, A.A. Advances in coated urea technology: Toward climate-responsive, microbiome-friendly, and site-specific nitrogen management. *J. Soil Sci. Plant Nutr.* **2026**, *26*, 6295–6313. [CrossRef]
80. Gurkok, S.; Ozdal, M.; Cakici, T.; Kurbanoglu, E.B. Antimicrobial, antibiofilm, and antiurease activities of green-synthesized Zn, Se, and ZnSe nanoparticles against *Streptococcus salivarius* and *Proteus mirabilis*. *Bioprocess. Biosyst. Eng.* **2025**, *48*, 589–603. [CrossRef] [PubMed]
81. Obaid, A.N.; Abdelghany, T.M.; Soliman, A.M. Green mycosynthesis of a CuO/ZnO heterojunction nanocomposite using *Aspergillus terreus* and its antibacterial and antivirulence activity against multidrug-resistant pathogens. *Sci. Rep.* **2026**, *16*, 12350. [CrossRef] [PubMed]
82. Goda, R.M.; Maghrabi, I.A.; El-Badawy, M.F.; Kabel, A.M.; Omar, A.A.; El-Morsi, R.M.; Ramadan, H.A.; Shohayeb, M.M. Developing a urinary catheter with anti-biofilm coated surface using phyto-assisted synthesis of zinc oxide nanoparticles. *Infect. Drug Resist.* **2025**, *18*, 1881–1893. [CrossRef] [PubMed]
83. Liu, S.; Qian, L.; Wu, Y.; Zhou, L.; Xu, X.; Yang, J.; Liu, C. Enhanced long-term performance of ureteral stents with functional coating: Combating bacterial adhesion and inhibiting encrustation. *Prog. Org. Coat.* **2024**, *192*, 108512. [CrossRef]
84. Herdiana, Y.; Wathoni, N.; Shamsuddin, S.; Muchtaridi, M. Drug release study of chitosan-based nanoparticles. *Heliyon* **2022**, *8*, e08674. [CrossRef] [PubMed]
85. Weng, J.; Durand, A.; Desobry, S. Chitosan-based particulate carriers: Structure, production, and controlled release. *Pharmaceutics* **2023**, *15*, 1455. [CrossRef] [PubMed]
86. Farasati Far, B.; Omrani, M.; Naimi Jamal, M.R. Multi-responsive chitosan-based hydrogels for controlled release of vincristine. *Commun. Chem.* **2023**, *6*, 28. [CrossRef] [PubMed]

87. Desai, N.; Rana, D.; Salave, S.; Gupta, R.; Patel, P. Chitosan: A potential biopolymer in drug delivery and biomedical applications. *Pharmaceutics* **2023**, *15*, 1313. [CrossRef] [PubMed]
88. Guimarães, M.; Gomes, G.M.; Santos, K.F. Morphological analysis reveals the influence of genipin and polyvinyl alcohol on porous morphology of interpenetrated chitosan xerogels. *Int. J. Adv. Mater. Biol. Mater.* **2024**, *6*, 47–60. [CrossRef]
89. Yilmaz, E.; Usturk, S.; Yılmaz, O.; Özbilenler, C. Chitosan hydrogels. In *Chitosan-Based Materials in Biomedical Applications*; Elsevier: Amsterdam, The Netherlands, 2026. [CrossRef]
90. Kiran, N.S.; Chatterjee, A.; Singh, S.; Yashaswini, C.; Prajapati, B.G. Biogenic metallic nanostructure coating for prevention and control of biofilm over surgical devices and food contact surfaces: A review. *Regen. Eng. Transl. Med.* **2026**. [CrossRef]
91. Xie, X.; Xu, K.; Su, X.; Zhang, Y.; Huang, Y.; Peng, X. A multifunctional textile coating for high-performance antibacterial applications via synergistic photothermal therapy, metal-ion sterilization, and antibacterial surface engineering. *Appl. Mater. Today* **2026**, *48*, 103057. [CrossRef]
92. Ahmed, A.S. Surface Modification of Copper-Based Alloys in Antibacterial Application. Ph.D. Thesis, Saarland University, Saarbrücken, Germany, 2025.
93. Bhattacharyya, S. Unveiling Janus Particle–Bacteria Interactions towards Nano-Antibiotics Development. Doctoral Dissertation, Indiana University, Bloomington, IN, USA, 2026.
94. Gauhar, V.; Castellani, D.; Teoh, J.Y.C.; Nedbal, C. Catheter-associated urinary tract infections and consequences of coated versus non-coated urethral catheters: Outcomes of a systematic review and meta-analysis. *J. Clin. Med.* **2022**, *11*, 4463. [CrossRef] [PubMed]
95. Rochester, M.; Rennie, C.; Hayes, C.; O'Driscoll, J.; Belci, M. A prospective multicenter randomized study to assess the impact of a novel catheter coating on clinical bacteriuria. *Antibiotics* **2026**, *15*, 369. [CrossRef] [PubMed]
96. Chadha, J.; Thakur, N.; Chhibber, S. A comprehensive status update on modification of Foley catheters to combat catheter-associated urinary tract infections and microbial biofilms. *Crit. Rev. Microbiol.* **2024**, *50*, 168–195. [CrossRef] [PubMed]

Disclaimer/Publisher's Note: The statements, opinions and data contained in all publications are solely those of the individual author(s) and contributor(s) and not of MDPI and/or the editor(s). MDPI and/or the editor(s) disclaim responsibility for any injury to people or property resulting from any ideas, methods, instructions or products referred to in the content.